Tests of Enhanced Leading Order QCD in W Boson plus Jets Events from 1.8 TeV $\overline{p}p$ Collisions

T. Affolder,[22] H. Akimoto,[44] A. Akopian,[37] M. G. Albrow,[10] P. Amaral,[7] S. R. Amendolia,[33] D. Amidei,[25] K. Anikeev,[23] J. Antos,[1] G. Apollinari,[10] T. Arisawa,[44] T. Asakawa,[42] W. Ashmanskas,[7] F. Azfar,[30] P. Azzi-Bacchetta,[31] N. Bacchetta,[31] M. W. Bailey,[27] S. Bailey,[15] P. de Barbaro,[36] A. Barbaro-Galtieri,[22] V. E. Barnes,[35] B. A. Barnett,[18] M. Barone,[12] G. Bauer,[23] F. Bedeschi,[33] S. Belforte,[41] W. H. Bell,[14] G. Bellettini,[33] J. Bellinger,[45] D. Benjamin,[9] J. Bensinger,[4] A. Beretvas,[10] J. P. Berge,[10] J. Berryhill,[7] B. Bevensee,[32] A. Bhatti,[37] M. Binkley,[10] D. Bisello,[31] M. Bishai,[10] R. E. Blair,[2] C. Blocker,[4] K. Bloom,[25] B. Blumenfeld,[18] S. R. Blusk,[36] A. Bocci,[33] A. Bodek,[36] W. Bokhari,[32] G. Bolla,[35] Y. Bonushkin,[5] D. Bortoletto,[35] J. Boudreau,[34] A. Brandl,[27] S. van den Brink,[18] C. Bromberg,[26] M. Brozovic,[9] N. Bruner,[27] E. Buckley-Geer,[10] J. Budagov,[8] H. S. Budd,[36] K. Burkett,[15] G. Busetto,[31] A. Byon-Wagner,[10] K. L. Byrum,[2] P. Calafiura,[22] M. Campbell,[25] W. Carithers,[22] J. Carlson,[25] D. Carlsmith,[45] J. Cassada,[36] A. Castro,[31] D. Cauz,[41] A. Cerri,[33] A. W. Chan,[1] P. S. Chang,[1] P. T. Chang,[1] J. Chapman,[25] C. Chen,[32] Y. C. Chen,[1] M. -T. Cheng,[1] M. Chertok,[39] G. Chiarelli,[33] I. Chirikov-Zorin,[8] G. Chlachidze,[8] F. Chlebana,[10] L. Christofek,[17] M. L. Chu,[1] Y. S. Chung,[36] C. I. Ciobanu,[28] A. G. Clark,[13] A. Connolly,[22] J. Conway,[38] J. Cooper,[10] M. Cordelli,[12] J. Cranshaw,[40] D. Cronin-Hennessy,[9] R. Cropp,[24] R. Culbertson,[10] D. Dagenhart,[43] S. D'Auria,[14] F. DeJongh,[10] S. Dell'Agnello,[12] M. Dell'Orso,[33] L. Demortier,[37] M. Deninno,[3] P. F. Derwent,[10] T. Devlin,[38] J. R. Dittmann,[10] S. Donati,[33] J. Done,[39] T. Dorigo,[15] N. Eddy,[17] K. Einsweiler,[22] J. E. Elias,[10] E. Engels, Jr.,[34] D. Errede,[17] S. Errede,[17] Q. Fan,[36] R. G. Feild,[46] J. P. Fernandez,[10] C. Ferretti,[33] R. D. Field,[11] I. Fiori,[3] B. Flaugher,[10] G. W. Foster,[10] M. Franklin,[15] J. Freeman,[10] J. Friedman,[23] Y. Fukui,[21] I. Furic,[23] S. Galeotti,[33] M. Gallinaro,[37] T. Gao,[32] M. Garcia-Sciveres,[22] A. F. Garfinkel,[35] P. Gatti,[31] C. Gay,[46] D. W. Gerdes,[25] P. Giannetti,[33] I. Gorelov,[27] P. Giromini,[12] V. Glagolev,[8] M. Gold,[27] J. Goldstein,[10] A. Gordon,[15] A. T. Goshaw,[9] Y. Gotra,[34] K. Goulianos,[37] C. Green,[35] P. Gris,[10] L. Groer,[38] C. Grosso-Pilcher,[7] M. Guenther,[35] G. Guillian,[25] J. Guimaraes da Costa,[15] R. S. Guo,[1] R. M. Haas,[11] C. Haber,[22] E. Hafen,[23] S. R. Hahn,[10] C. Hall,[15] T. Handa,[16] R. Handler,[45] W. Hao,[40] F. Happacher,[12] K. Hara,[42] A. D. Hardman,[35] R. M. Harris,[10] F. Hartmann,[19] K. Hatakeyama,[37] J. Hauser,[5] J. Heinrich,[32] A. Heiss,[19] M. Herndon,[18] K. D. Hoffman,[35] C. Holck,[32] R. Hollebeek,[32] L. Holloway,[17] R. Hughes,[28] J. Huston,[26] J. Huth,[15] H. Ikeda,[42] J. Incandela,[10] G. Introzzi,[33] J. Iwai,[44] Y. Iwata,[16] E. James,[25] H. Jensen,[10] M. Jones,[32] U. Joshi,[10] H. Kambara,[13] T. Kamon,[39] T. Kaneko,[42] K. Karr,[43] H. Kasha,[46] Y. Kato,[29] T. A. Keaffaber,[35] K. Kelley,[23] M. Kelly,[25] R. D. Kennedy,[10] R. Kephart,[10] D. Khazins,[9] T. Kikuchi,[42] B. Kilminster,[36] B. J. Kim,[20] D. H. Kim,[20] H. S. Kim,[17] M. J. Kim,[20] S. H. Kim,[42] Y. K. Kim,[22] M. Kirby,[9] M. Kirk,[4] L. Kirsch,[4] S. Klimenko,[11] P. Koehn,[28] A. Köngeter,[19] K. Kondo,[44] J. Konigsberg,[11] K. Kordas,[24] A. Korn,[23] A. Korytov,[11] E. Kovacs,[2] J. Kroll,[32] M. Kruse,[36] S. E. Kuhlmann,[2] K. Kurino,[16] T. Kuwabara,[42] A. T. Laasanen,[35] N. Lai,[7] S. Lami,[37] S. Lammel,[10] J. I. Lamoureux,[4] M. Lancaster,[22] G. Latino,[33] T. LeCompte,[2] A. M. Lee IV,[9] K. Lee,[40] S. Leone,[33] J. D. Lewis,[10] M. Lindgren,[5] T. M. Liss,[17] J. B. Liu,[36] Y. C. Liu,[1] N. Lockyer,[32] J. Loken,[30] M. Loreti,[31] D. Lucchesi,[31] P. Lukens,[10] S. Lusin,[45] L. Lyons,[30] J. Lys,[22] R. Madrak,[15] K. Maeshima,[10] P. Maksimovic,[15] L. Malferrari,[3] M. Mangano,[33] M. Mariotti,[31] G. Martignon,[31] A. Martin,[46] J. A. J. Matthews,[27] J. Mayer,[24] P. Mazzanti,[3] K. S. McFarland,[36] P. McIntyre,[39] E. McKigney,[32] M. Menguzzato,[31] A. Menzione,[33] C. Mesropian,[37] A. Meyer,[7] T. Miao,[10] R. Miller,[26] J. S. Miller,[25] H. Minato,[42] S. Miscetti,[12] M. Mishina,[21] G. Mitselmakher,[11] N. Moggi,[3] E. Moore,[27] R. Moore,[25] Y. Morita,[21] M. Mulhearn,[23] A. Mukherjee,[10] T. Muller,[19] A. Munar,[33] P. Murat,[10] S. Murgia,[26] J. Nachtman,[5] S. Nahn,[46] H. Nakada,[42] T. Nakaya,[7] I. Nakano,[16] C. Nelson,[10] T. Nelson,[10] D. Neuberger,[19] C. Newman-Holmes,[10] C.-Y. P. Ngan,[23] P. Nicolaidi,[41] H. Niu,[4] L. Nodulman,[2] A. Nomerotski,[11] S. H. Oh,[9] T. Ohmoto,[16] T. Ohsugi,[16] R. Oishi,[42] T. Okusawa,[29] J. Olsen,[45] W. Orejudos,[22] C. Pagliarone,[33] F. Palmonari,[33] R. Paoletti,[33] V. Papadimitriou,[40] S. P. Pappas,[46] D. Partos,[4] J. Patrick,[10] G. Pauletta,[41] M. Paulini,[(*) 22] C. Paus,[23] L. Pescara,[31] T. J. Phillips,[9] G. Piacentino,[33] K. T. Pitts,[17] A. Pompos,[35] L. Pondrom,[45] G. Pope,[34] M. Popovic,[24] F. Prokoshin,[8] J. Proudfoot,[2] F. Ptohos,[12] O. Pukhov,[8] G. Punzi,[33] K. Ragan,[24] A. Rakitine,[23] D. Reher,[22] A. Reichold,[30] A. Ribon,[31] W. Riegler,[15] F. Rimondi,[3] L. Ristori,[33] M. Riveline,[24] W. J. Robertson,[9] A. Robinson,[24] T. Rodrigo,[6] S. Rolli,[43] L. Rosenson,[23] R. Roser,[10] R. Rossin,[31] A. Safonov,[37] R. St. Denis,[14] W. K. Sakumoto,[36] D. Saltzberg,[5] A. Sansoni,[12] L. Santi,[41] H. Sato,[42] P. Savard,[24] P. Schlabach,[10] E. E. Schmidt,[10] M. P. Schmidt,[46] M. Schmitt,[15] L. Scodellaro,[31] A. Scott,[5] A. Scribano,[33] S. Segler,[10] S. Seidel,[27] Y. Seiya,[42] A. Semenov,[8] F. Semeria,[3] T. Shah,[23] M. D. Shapiro,[22] P. F. Shepard,[34] T. Shibayama,[42] M. Shimojima,[42] M. Shochet,[7] J. Siegrist,[22] G. Signorelli,[33] A. Sill,[40] P. Sinervo,[24] P. Singh,[17] A. J. Slaughter,[46] K. Sliwa,[43] C. Smith,[18] F. D. Snider,[10] A. Solodsky,[37] J. Spalding,[10] T. Speer,[13] P. Sphicas,[23] F. Spinella,[33] M. Spiropulu,[15] L. Spiegel,[10] J. Steele,[45] A. Stefanini,[33] J. Strologas,[17] F. Strumia, [13] D. Stuart,[10] K. Sumorok,[23] T. Suzuki,[42] T. Takano,[29] R. Takashima,[16] K. Takikawa,[42] P. Tamburello,[9] M. Tanaka,[42] B. Tannenbaum,[5] W. Taylor,[24] M. Tecchio,[25] P. K. Teng,[1] K. Terashi,[37] S. Tether,[23]

D. Theriot,[10] A. S. Thompson,[14] R. Thurman-Keup,[2] P. Tipton,[36] S. Tkaczyk,[10] K. Tollefson,[36] A. Tollestrup,[10] H. Toyoda,[29] W. Trischuk,[24] J. F. de Troconiz,[15] J. Tseng,[23] N. Turini,[33] F. Ukegawa,[42] T. Vaiciulis,[36] J. Valls,[38] S. Vejcik III,[10] G. Velev,[10] R. Vidal,[10] R. Vilar,[6] I. Volobouev,[22] D. Vucinic,[23] R. G. Wagner,[2] R. L. Wagner,[10] J. Wahl,[7] N. B. Wallace,[38] A. M. Walsh,[38] C. Wang,[9] C. H. Wang,[1] M. J. Wang,[1] T. Watanabe,[42] D. Waters,[30] T. Watts,[38] R. Webb,[39] H. Wenzel,[19] W. C. Wester III,[10] A. B. Wicklund,[2] E. Wicklund,[10] H. H. Williams,[32] P. Wilson,[10] B. L. Winer,[28] D. Winn,[25] S. Wolbers,[10] D. Wolinski,[25] J. Wolinski,[26] S. Wolinski,[25] S. Worm,[27] X. Wu,[13] J. Wyss,[33] A. Yagil,[10] W. Yao,[22] G. P. Yeh,[10] P. Yeh,[1] J. Yoh,[10] C. Yosef,[26] T. Yoshida,[29] I. Yu,[20] S. Yu,[32] Z. Yu,[46] A. Zanetti,[41] F. Zetti,[22] and S. Zucchelli[3]

(CDF Collaboration)

[1] *Institute of Physics, Academia Sinica, Taipei, Taiwan 11529, Republic of China*
[2] *Argonne National Laboratory, Argonne, Illinois 60439*
[3] *Istituto Nazionale di Fisica Nucleare, University of Bologna, I-40127 Bologna, Italy*
[4] *Brandeis University, Waltham, Massachusetts 02254*
[5] *University of California at Los Angeles, Los Angeles, California 90024*
[6] *Instituto de Fisica de Cantabria, CSIC-University of Cantabria, 39005 Santander, Spain*
[7] *Enrico Fermi Institute, University of Chicago, Chicago, Illinois 60637*
[8] *Joint Institute for Nuclear Research, RU-141980 Dubna, Russia*
[9] *Duke University, Durham, North Carolina 27708*
[10] *Fermi National Accelerator Laboratory, Batavia, Illinois 60510*
[11] *University of Florida, Gainesville, Florida 32611*
[12] *Laboratori Nazionali di Frascati, Istituto Nazionale di Fisica Nucleare, I-00044 Frascati, Italy*
[13] *University of Geneva, CH-1211 Geneva 4, Switzerland*
[14] *Glasgow University, Glasgow G12 8QQ, United Kingdom*
[15] *Harvard University, Cambridge, Massachusetts 02138*
[16] *Hiroshima University, Higashi-Hiroshima 724, Japan*
[17] *University of Illinois, Urbana, Illinois 61801*
[18] *The Johns Hopkins University, Baltimore, Maryland 21218*
[19] *Institut für Experimentelle Kernphysik, Universität Karlsruhe, 76128 Karlsruhe, Germany*
[20] *Korean Hadron Collider Laboratory: Kyungpook National University, Taegu 702-701; Seoul National University, Seoul 151-742; and SungKyunKwan University, Suwon 440-746; Korea*
[21] *High Energy Accelerator Research Organization (KEK), Tsukuba, Ibaraki 305, Japan*
[22] *Ernest Orlando Lawrence Berkeley National Laboratory, Berkeley, California 94720*
[23] *Massachusetts Institute of Technology, Cambridge, Massachusetts 02139*
[24] *Institute of Particle Physics: McGill University, Montreal H3A 2T8; and University of Toronto, Toronto M5S 1A7; Canada*
[25] *University of Michigan, Ann Arbor, Michigan 48109*
[26] *Michigan State University, East Lansing, Michigan 48824*
[27] *University of New Mexico, Albuquerque, New Mexico 87131*
[28] *The Ohio State University, Columbus, Ohio 43210*
[29] *Osaka City University, Osaka 588, Japan*
[30] *University of Oxford, Oxford OX1 3RH, United Kingdom*
[31] *Universita di Padova, Istituto Nazionale di Fisica Nucleare, Sezione di Padova, I-35131 Padova, Italy*
[32] *University of Pennsylvania, Philadelphia, Pennsylvania 19104*
[33] *Istituto Nazionale di Fisica Nucleare, University and Scuola Normale Superiore of Pisa, I-56100 Pisa, Italy*
[34] *University of Pittsburgh, Pittsburgh, Pennsylvania 15260*
[35] *Purdue University, West Lafayette, Indiana 47907*
[36] *University of Rochester, Rochester, New York 14627*
[37] *Rockefeller University, New York, New York 10021*
[38] *Rutgers University, Piscataway, New Jersey 08855*
[39] *Texas A&M University, College Station, Texas 77843*
[40] *Texas Tech University, Lubbock, Texas 79409*
[41] *Istituto Nazionale di Fisica Nucleare, University of Trieste/ Udine, Italy*
[42] *University of Tsukuba, Tsukuba, Ibaraki 305, Japan*
[43] *Tufts University, Medford, Massachusetts 02155*
[44] *Waseda University, Tokyo 169, Japan*
[45] *University of Wisconsin, Madison, Wisconsin 53706*
[46] *Yale University, New Haven, Connecticut 06520*
[(*)] *Now at Carnegie Mellon University, Pittsburgh, Pennsylvania 15213*

(August 11, 2000)

We present a study of events with W bosons and hadronic jets produced in $\overline{p}p$ collisions at a center of mass energy of 1.8 TeV. The data consist of 51400 $W \rightarrow e\nu$ decay candidates from 108 pb^{-1} of integrated luminosity collected using the CDF detector at the Fermilab Tevatron Collider. Cross sections and jet production properties have been measured for $W + \geq 1$ to ≥ 4 jet events. The data compare well to predictions of leading-order QCD matrix element calculations with added gluon radiation and simulated parton fragmentation.

I. INTRODUCTION

The production of W bosons in $\overline{p}p$ collisions at the Fermilab Tevatron Collider provides the opportunity to test perturbative QCD predictions at large momentum transfers. A sample of 51400 W candidates collected from 108 pb^{-1} of accumulated data is used to study the kinematic properties and production rates of high energy hadronic jets produced in association with W bosons. The jets are produced from high-energy partons (quarks and gluons) when they hadronize after the collision. Figure 1 shows some of the Leading-Order (LO) processes which produce a W boson and a jet. The well understood electroweak decays $W \to e\nu$ of the W boson provide efficient identification of W candidates with low background contamination. These electronic W decays provide sufficient statistics to study the QCD production characteristics for $W+ \geq 0$ to ≥ 4 jet event samples.

In this paper we first describe the data analysis techniques used to measure the production cross section and kinematic properties of $W+ \geq n$ jets events. We then describe a Leading-Order perturbative QCD calculation which is enhanced with a coherent shower evolution of both initial- and final-state partons, hadronization, and inclusion of a data-based soft underlying event model. We refer to this tree level calculation interfaced with parton evolution as Enhanced Leading Order (ELO). Similar ELO QCD calculations are commonly used for generating predictions of a variety of important physics processes including top production, diboson production, higgs production and SUSY processes. We use the high statistics single W boson data sample to assess the performance of these calculations over a large jet energy domain and over a range of jet multiplicities.

Published analyses that use similar data to study W production and decay properties are found in references [1–4] for single boson production, [5–7] for diboson (WW, WZ, $W\gamma$) production, and [8–10] for the pair production of top quarks. Additional information about this analysis can be found in [11]. Our goal in the current analysis is a comprehensive study of W boson production and the reliability of perturbative QCD in predicting the data over a range of jet energies and jet multiplicity at the highest center of mass energies studied to date.

II. THE COLLIDER DETECTOR AT FERMILAB

This analysis uses data collected at the Collider Detector at Fermilab (CDF), a multi-purpose detector designed for precision energy, momentum, and position measurements of particles produced in $\sqrt{s} = 1.8$ TeV $\overline{p}p$ collisions. A diagram of the CDF detector is shown in Figure 2. The CDF detector is described in more detail in [12] and references therein. The focus here will be those elements useful in identifying the final state particles of $W \to e\nu$ + jet events.

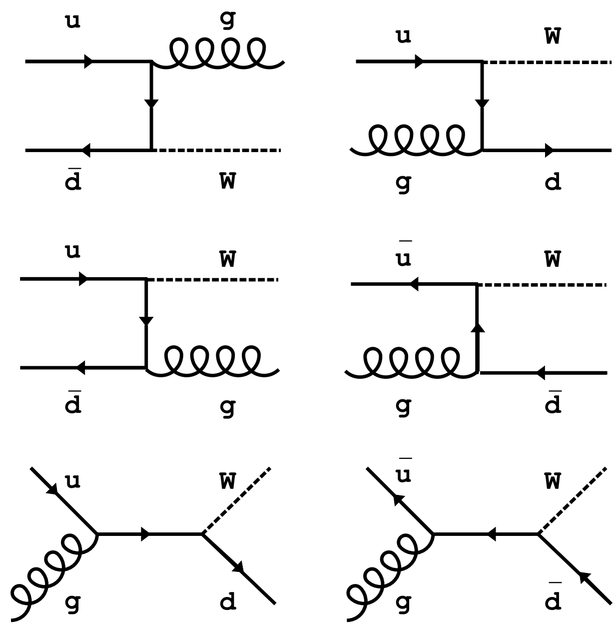

FIG. 1. Feynman diagrams for some of the leading-order processes that produce a W boson with an associated jet. Additional diagram can be obtained by exchanging the u and the d quarks, or by replacing them with other pairs of quarks.

The coordinate system at CDF is defined with respect to the proton beam direction. The positive z direction is the proton beam direction and ϕ is the azimuthal angle and is measured around the beam axis. The polar angle θ is the angle from the proton beam. An alternative variable to θ is the *pseudorapidity* which is defined by $\eta = -\log(\tan(\theta/2))$. The transverse component of energy (E_T) and momentum (P_T) of a particle is the projection into the plane transverse to the beam line.

The principle detectors used in analyzing these events are the vertex detector (VTX), the central tracking chamber (CTC) and the full set of hadronic and electromagnetic calorimeters. The VTX is a time projection drift chamber which allows us to reconstruct the position along the beam line where a W boson is produced. Reliable vertex reconstruction permits us to reconstruct multiple vertices from additional $\overline{p}p$ interactions that occur simultaneous with the primary $\overline{p}p$ collision. Knowledge of additional $\overline{p}p$ interactions allows us to correct for energy contamination due to additional inelastic $\overline{p}p$ collisions. The CTC is a open cell drift chamber which precisely measures a particle's trajectory over a 1.4 meter radius from the beam line. The curvature of the trajectory and the known solenoidal magnetic field gives a measurement of the charged particle's momentum.

The most accurate measurement of a W electron's energy is derived from the central electromagnetic calorimeter (CEM). The CEM is a lead-scintillator calorimeter with 2π azimuthal coverage and pseudorapidity coverage of $|\eta| \leq 1.0$. The finest segmentation of the electromag-

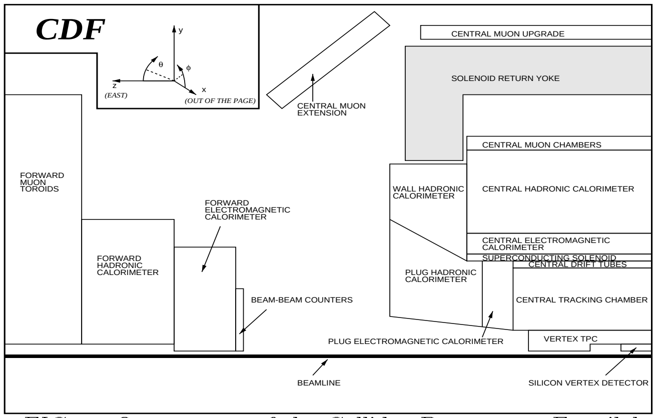

FIG. 2. One quarter of the Collider Detector at Fermilab. The major detector elements are indicated. The center of the detector is along the beam line to the far right.

TABLE I. Estimate of the $W \to e\nu$ sample size. Each entry includes all the conditions on earlier lines, except for the background (last entry) which adds events not coming from above.

Sample	Number of Events
$\overline{p}p$ interactions	5.5×10^{12}
W produced	2.9×10^{6}
W decays to $e\nu$	2.7×10^{5}
e is central	1.5×10^{5}
e is fiducial	1.1×10^{5}
electron $E_T \geq 20$ GeV	9.4×10^{4}
electron ID	8.3×10^{4}
$\not{E}_T \geq 30$ GeV	5.4×10^{4}
Jet overlap, etc.	4.8×10^{4}
background	5.1×10^{4}

netic calorimeter is referred to as a tower with each tower covering 15° in phi and 0.1 units of η yielding a total of 480 towers. Each tower energy measurement is read independently by a pair of phototubes. The electron energy resolution for the CEM is $0.137/\sqrt{E \cdot \sin\theta} \oplus 0.02$ where E is in GeV.

The CEM and CTC together provide several discrimination tests that are used to separate electrons from other physics objects such as photons and jets. These are described in the next section.

Jets are measured primarily in the calorimeters. The central hadronic calorimeter (CHA) is behind the CEM and consists of alternating iron and scintillator sheets with segmentation that matches the CEM. The energy resolution of the CHA is $0.5/\sqrt{E \cdot \sin\theta} \oplus 0.03$. The large size of typical jets combined with the fine segmentation of the calorimeter means that the jet energy is generally spread over many towers. This analysis included jets out to $|\eta| \leq 2.4$, so the jet energy can also be in the plug and forward calorimeters. These calorimeters are similar to the CEM and CHA with the exceptions that the scintillators are replaced with wire proportional chambers, and ϕ is segmented in 5° sections rather than in 15° sections.

III. W BOSON IDENTIFICATION

CDF excels at electron identification and precision electron energy measurement, and we use this ability to select a clean sample of events containing high energy electrons. We describe both the kinematic selection of the electrons and the discrimination variables that are employed to distinguish electrons from other types of energy. The inclusive electron sample will contain those electrons which were produced from a W decaying to electron plus neutrino. A W sample can be extracted from the electron sample by the identification of the neutrino. The result of high energy electron and neutrino selection is a 94% pure sample of W bosons.

The W sample is divided into subsamples according to the number of jets produced with the boson. In contrast to the electron, the definition of a jet is more of an analysis decision. Jets produced with a W can have essentially any energy and the jet's pattern of energy deposition varies from jet to jet. However, if the jet energy is corrected to represent the energy of the parent parton, a precise definition is a matter of the capabilities of the detector and the validity of the theoretical predictions at the minimum allowed jet energy. The analysis requirements used in defining a jet are presented in section IV.

A. Electron Selection

1. Trigger Path

During data collection in the period from 1992 to 1995 at the Collider Detector at Fermilab, there were about 5.5 trillion $\overline{p}p$ interactions in the detector's collision region, and in only about 3 million of these events were W bosons produced. Nine percent of these W bosons decayed to the desired final state ($e\nu$). In order to reduce the events recorded for analysis and enhance the fraction of recorded events with interesting physics, we employ a series of online triggers. The $W+$ jet analysis uses a trigger path that is designed to identify events with a high transverse energy central ($|\eta| \leq 1.2$) electron. This sample contains $W \to e\nu$ decays along with a variety of other inclusive electron processes. The electron trigger data sample is used as the starting point for the offline analysis.

For most of Run 1, the level-one triggers were the first of a series for filtering the hard scattering events from $\overline{p}p$ collisions. One level-one calorimeter trigger required that an event deposit a minimum transverse energy of 8 GeV in a central-electromagnetic calorimeter tower. The W boson selection relies only on this level-one trigger.

Events which pass the level-one triggers are evaluated at level two. In our analysis, we require that an event pass the level-two combined central electron trigger. This trigger consists of 16 individual central-electron triggers; however, our data sample depends predominately on the high E_T electron trigger which requires a electromagnetic transverse energy (E_T(EM)) of 16 GeV and a track of momentum 12 GeV/c. The fraction of hadronic energy in the associated hadronic towers is required to be small ($< 0.125 \cdot E_T$(EM)) in order to reduce the contamination caused by jets which pass the trigger. The allowed η range for the energy deposition is ± 1.19.

The third trigger level uses reconstructed data so that specific physics decisions can be made. We use an inclusive electron level-three trigger which allows us to later select W and Z bosons from a common trigger sample so that the systematic errors in efficiencies are common. The most important inclusive trigger we use has higher track momentum (13.0 GeV/c) and higher electromagnetic energy (18.0 GeV) requirements than the level-two trigger. This trigger also requires that the 3D track point to the calorimeter energy thus identifying electrons and rejecting photon events with incidental tracks in the event.

With our level-two and level-three trigger requirements, the efficiency of identifying a $W \to e\nu$ decay where the electron has an $E_T \geq$ 20 GeV in the central detector and will pass our electron quality requirements (described in the next section) is greater than 99%. However, the W purity of the sample is still too low to be useful for our analysis, so we need to employ a series of analysis requirements designed to enhance the component of electrons which come from $W \to e\nu$ decays.

2. Electron Geometric, Kinematic and Quality Requirements

The electron trigger sample is reprocessed with offline reconstruction code. After reconstruction we apply the tight central electron selection requirements [13]. The list that follows details this selection.

The first five requirements described below represent geometric and kinematic requirements on the electron energy. The additional requirements are predominately quality variables designed to discriminate between electron and non-electron energy depositions. The total W selection efficiency of the additional requirements is about 85% yet they reduce the number of events in the sample by about 90%.

Central: The allowed η range of the EM energy is $\pm$ 1.1 which is determined by the central electromagnetic calorimeter coverage. Limiting the pseudorapidity range of the electron allows precise electron energy measurements and low background contamination. This requirement selects about 55% of the $W \to e\nu$ events. $z = 0$ is taken at the center of the detector for fiducial requirements and at the interaction vertex for event variables.

Fiducial: We restrict electrons to be in well-instrumented regions of the central electromagnetic calorimeters (CEM). About 75% of the area of the CEM is suitable for precision EM energy measurements.

Interaction Vertex (z_{vtx}): A W boson can be produced anywhere the proton and antiproton bunches overlap. Figure 3 shows the distribution in z_{vtx} of the primary vertex. The zero of the plot is the center of the detector. To keep the interaction inside the fiducial volume of the detector and to maintain the calorimeter's projective tower geometry we require the W boson interaction vertex to be within 60 cm of the center of the detector. Several vertices can be reconstructed for an event. To identify the W boson vertex we choose the vertex closest to the track of the electron from the W decay. In the rare event that no vertex is within 5 cm of the electron track we use the electron's track to determine the z position of the interaction.

Electron-Jet Separation ΔR_{ej}: Electron activity and high E_T jet activity are kept clearly separated in the analysis with an electron-jet separation requirement. We reject all events which have a jet which passes our selection criteria (described in Section IV and is centered in an η–ϕ cone of radius R=0.52 around the electron.

High electron E_T: The E_T of the electron is corrected at the offline analysis level for all known detector effects. We require the corrected electron E_T to be greater than 20 GeV thus avoiding trigger threshold effects. About 85% of central electrons from W decay have E_T greater than 20 GeV.

Isolation (Iso): An effective electron quality requirement we use is the requirement that the electromagnetic energy be physically separated from other energy in the detector. The isolation is defined as the ratio of all non-electron energy in a cone of 0.4 around the electron to the electron energy.

$$Iso = \frac{E_T(0.4) - E_T(electron)}{E_T(electron)}$$

A cone is defined by the center of the electron energy deposition and a maximum radius ($R = (\Delta\eta^2 + \Delta\phi^2)^{1/2}$) in which we look for non-electron energy. Non-electron energy includes both hadronic and electromagnetic calorimetry energy that is not contained in the electron tower(s). The non-electron energy is required to be no more than 10% of the electron energy (Iso $\leq$ 0.1). The Isolation requirement reduces the background from electron-like jets. The isolation distribution is shown in Figure 3.

Hadronic Energy Fraction (Had/EM): To further suppress mis-identification of jets as electrons, we check the hadronic calorimeter towers that are behind the electromagnetic towers that contain the electron's energy. Leakage of the electrons energy into the hadronic towers is a function of the electrons energy. We limit the ratio of hadronic over electromagnetic energy by the formula

$$Had/EM < 0.055 + 0.00045 \cdot E_{ele}$$

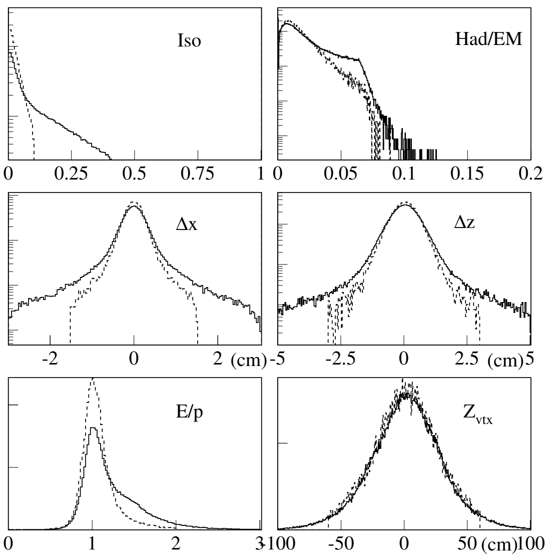

FIG. 3. Distributions of some of the quality variables which are used to isolate high E_T central electrons that result from W decay. The solid histograms show the variables before the requirements are applied. The dashed histograms show the variables after full electron selection, normalized to the same (arbitrary) area. The variables plotted are the following: electron isolation (Iso), hadronic over electromagnetic energy (Had/EM), CTC and CES matching in *local* x (Δx) and along z (Δz), electron energy divided by electron momentum (E/p) and the vertex distribution (z_{vtx}).

where the units for E_{ele} are in GeV. The Had/EM distribution is shown in Figure 3.

Lateral Energy Sharing: The electron's energy is generally spread over more than one tower. The lateral energy sharing variable (L_{share}) compares the expected and measured lateral leakage from the electron seed tower to the adjacent towers. This is required to be consistent with the sharing expected for an electron.

High P_T: Since electrons and photons have similar calorimetry signatures, we require a track pointing to the EM energy deposit with a P_T of at least 13.0 GeV to remove high-E_T photons.

Strip Chamber Variables (χ^2_{str},Δx,Δz): The central strip chamber (CES) embedded in the EM calorimeter provides a transverse profile of the electron shower at the expected shower maximum. The profile is compared to an expected electron profile shape which is determined from test beam data. The χ^2 of this shape comparison is used as a discrimination variable. The strip profile is also used to determine the position of the electron inside the calorimeter tower. The position resolution is 0.17 cm for a 50 GeV electron in the CES. CES position measurements are compared to those obtained from the track in the central tracking chamber. These are required to match within 1.5 cm in the $R \cdot \phi$ (Δx) direction and 3.0 cm in the z direction (Δz). Distributions for Δx and Δz are shown in Figure 3.

Energy Momentum Ratio (E/p): The ratio of energy and momentum of a relativistic electron is usually close to one. We require the ratio of measured energy to measured momentum to be between 0.5 and 2.0. Figure 3 shows this ratio for our inclusive electron sample. The long tail on the high side is from low electron momentum measurements due to Bremsstrahlung radiation of the electron where the radiated energy is collinear with the electron and is deposited in the same calorimeter tower as the electron.

Conversion Rejection: High energy photons converting to electron-positron pairs can fake an electron from a W decay. Photon conversions can be identified and removed directly by reconstructing the conversion vertex of a pair of oppositely charged tracks. In addition, if the photon converts outside the radius of the vertex chamber there will be a deficit of wire hits in the VTX along the direction pointing to the CTC track. We require that the observed number of VTX hits be at least 20% of the expected number of hits when at least 8 wire hits are expected.

Run Quality: Each run of the accelerator is required to meet a set of minimum quality conditions. The beam conditions must be stable and the integrated luminosity delivered must be greater than 1.0 nb^{-1}. All detectors must be operational and the solenoid ramped to the correct current. Temperatures, voltages, trigger rates and electronics are required to be within operational limits. Additionally, the validation group at CDF checks physics distributions for any anomalous behavior that would indicate problems. We analyze only those runs which meet the run quality requirements for the detectors used here. We do not exclude runs with problems in the muon subsystems since we do not use these detectors in this analysis.

We use a subset of the selection requirements ("loose requirements") to select the electrons from the trigger sample and then the full selection ("tight requirements") to obtain our final electron sample. The main difference between the loose and the tight requirements is the isolation requirement in the tight selection, which strongly rejects electron-like jets from multijet events. The loosely selected sample is used to measure residual multijet contamination, described in section V B 3. The loose and tight selection requirements are both listed in Table II and the E_T distribution at both stages of selection are shown in Figure 4, which shows the enhancement of the W electron E_T peak as additional W selection requirements are applied.

B. Neutrino Selection

So far we have used the final state electron of $W \to e\nu$ events to tag the W boson. Of the processes that con-

TABLE II. List of quality requirements for $W \to e\nu$ selection.

requirement	loose	tight
Detector Region	Central	
fiducial volume	yes	
ΔR_{ej}	≥ 0.52	
E_T(corrected)	$\geq$ 20 GeV	
Iso(0.4)	—	≤ 0.1
Had/EM	$\leq 0.055 + 0.00045 E_{ele}$ (GeV)	
L_{shr}	≤ 0.2	
$P_T \geq$	13 GeV/c	
$\|\Delta x\|$	$\leq$ 3.0 cm	$\leq$ 1.5 cm
$\|\Delta z\|$	$\leq$ 5.0 cm	$\leq$ 3.0 cm
χ^2_{str}	≤ 10.0	
E/p	≤ 3.0	≥ 0.5 and ≤ 2.0
$\|z_{vtx}\|$	–	$\leq$ 60.0 cm
remove conversions	no	yes
require good run	no	yes

tribute to the inclusive high E_T electron sample, the $W \to e\nu$ decay is unique for its single final state high E_T neutrino. The neutrino does not interact with the detector components therefore its presence must be inferred by considering energy-momentum constraints on the event. The momentum components of the final state particles transverse to the beam line should sum to zero because the initial state particles have essentially zero net transverse momentum. Since the neutrino deposits no energy in the detector the vector sum of the measured transverse energies will not sum to zero. We refer to this imbalance of transverse energy as missing transverse energy ($\not{E}_T$).

The missing transverse energy is calculated using the corrected energies from electrons, muons, photons and jets. In addition, low-energy depositions are often scattered throughout the detector and must also be used in the missing transverse energy calculation. We refer to the low-energy component as unclustered energy, and its sources include underlying event energy from the spectator quarks in the W interaction, energy from partons which escape the jet clustering algorithm (out–of–cone), and energy from extra interactions. Extra interaction energy is of course not useful in constraining the neutrino energy since it arises from an independent interaction; however, we must accept it since we cannot separate it from the W event.

The jets are not corrected for radiation of energy out of the 0.4 cone. This is so we avoid double counting this energy which will appear in our unclustered-energy component. No attempt was made to subtract the underlying event energy from the jet cluster and add it to the unclustered energy.

After identification of jets in the event we remove the associated raw jet energy from the calorimeter towers. The electron energy is also removed, and the remaining energy defines the unclustered-energy component. We vectorially sum the individual calorimeter towers to obtain the unclustered-energy vector. A calorimeter tower contributes to this sum if it has at least 0.1 GeV of transverse energy, a threshold designed to match the jet clustering algorithm.

The above procedure results in the identification of the three components (electron, jet, and unclustered; in general these events do not contain muons) of missing transverse energy. Each component is individually corrected and the vector sum is calculated yielding the $\not{E}_T$

$$\vec{\not{E}_T} = -(\vec{E_{ele}} + \vec{E_{jet}} + K \cdot \vec{E_{unc}})$$

We have determined the value of K in this equation to be 2.0 by analyzing a sample of Z events where the true $\not{E}_T$ is expected to be zero.

C. W Selection

W events are selected by requiring both a high-quality electron (using the tight electron requirements) with $E_T \geq 20$ GeV and a high transverse energy neutrino with $\not{E}_T \geq 30$ GeV. Figure 5 shows the imbalance of transverse energy for our tight central electron sample and Figure 4 shows the change in the electron E_T distribution after the $\not{E}_T$ requirement is applied. Although the $\not{E}_T$ requirement selects only 65% of the W boson candidates, the purity of the final sample is 94%.

Z bosons which decay to electron-positron pairs will pass the same electron selection criteria as electrons (positrons) from W boson decay. While Z boson events are not expected to produce much $\not{E}_T$, measurement error can push the missing E_T above our threshold, especially for the higher jet multiplicity events. Therefore we must reject the $Z \to e^+e^-$ events by searching for them directly. Some care must be taken because we intend to identify jets in the W events and our Z identification should not strongly reject electron-jet combinations as being Z bosons thus biasing the sample against high jet multiplicity. The following Z identification requirements are applied to a second electron:

- Had/EM ≤ 0.125
- Iso(0.4) ≤ 0.1
- Central Detector: E_T (corrected) ≥ 20 GeV
- Plug Detector: E_T (corrected) ≥ 15 GeV
- Forward Detector: E_T (corrected) ≥ 10 GeV
- 76 GeV/$c^2 \leq M_{ee} \leq 106$ GeV/c^2

M_{ee} is the electron-positron invariant mass.

Applying all athe above selection criteria, we have 51431 candidate W boson events for our $W+$ jet analysis.

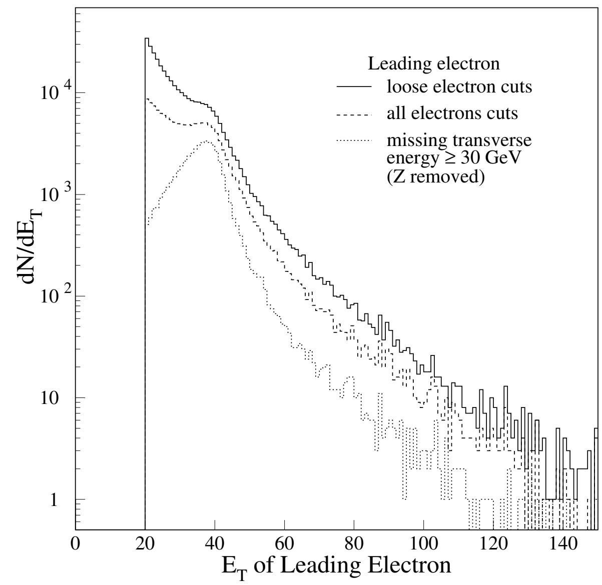

FIG. 4. The E_T distribution for events stripped with a subset of the electron selection requirements, full electron selection, and our final W sample which includes a missing transverse energy ($\not\!\!E_T$) requirement of at least 30 GeV.

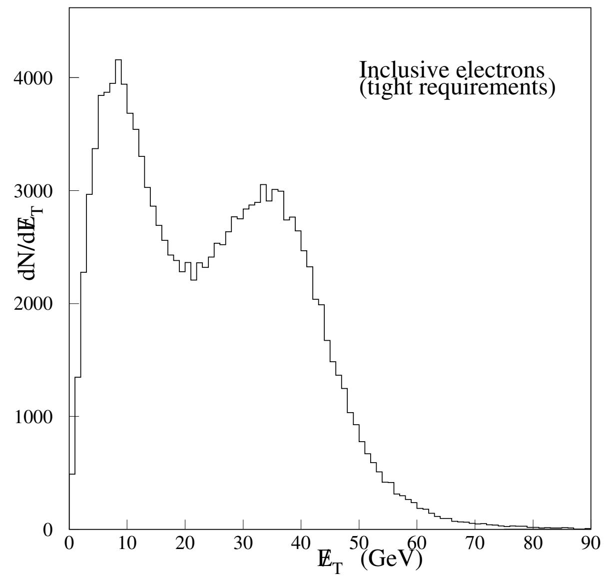

FIG. 5. The plot shows the $\not\!\!E_T$ distribution for the inclusive electron sample. Noticeable is the W peak due to the escaped ν.

IV. JET SELECTION AND CORRECTIONS

The requirements described in the previous section select a $W \to e\nu$ sample of 51431 events. We divide this sample into subsamples according to the number of jets produced along with the W boson. The process of $W+$ jet production can be factored into two steps: (1) The production of $W+$ n partons where a parton is a gluon or quark; and (2) the fragmentation and hadronization of the partons (quark/gluon $\to$ hadrons). The manifestation of high momentum parton production is therefore multiple hadrons in the detector which are generally clustered in a direction close to the direction of the parent-parton. The lego plot of Figure 6 shows a hadronic cluster of energy in the calorimeter. The cylindrical calorimeter has been sliced at $\phi = 0$ and unfolded for this plot. The vertical axis represents the transverse energy per tower. The electron energy is shaded darker. The jet cluster is evident and we see that its calorimetry signature is distinct from that of the electron cluster. Since jet shapes and energies vary dramatically from jet to jet we use a jet finding procedure that is capable of identifying potential jet candidates with a large range of shapes.

A. Jet Clustering

We use a cone clustering algorithm for finding jets [14]. In this procedure we look for a seed tower around which to cluster. Seed towers are all calorimeter towers containing more than 1.0 GeV of transverse energy. We search in a cone $R{=}(\Delta\phi^2 + \Delta\eta^2)^{1/2}$ around the seed tower and add any towers with an E_T more than 0.1 GeV. If the individual seed towers are closer than the cone radius they are merged. Thus several iterations are necessary before a stable set of clusters is found. On each iteration the centroids of the clusters are recalculated and used as the center of the cone for the next iteration.

We use a cone radius of 0.4 for the clustering algorithm. This choice is small enough for counting jets and is less susceptible to energy contamination from outside the jet as we discuss later. We also make three modifications to the standard clustering procedure. First, we remove the electron's energy from the towers before clustering, since the jet clustering procedure will identify electrons as jets. This electron suppression allows energy near the electron to be contained in the appropriate jet cluster. Secondly, we redefine the clustering vertex as the W boson vertex (see definition in section III A 2) if a discrepancy exists so that all transverse energy in the event is calculated from the W vertex. Finally, we merge any jets that have E_T above 12 GeV (after the corrections described below) and are separated by less than 0.52 in η-ϕ space. This factor represents a jet separation resolution criterion; it is quite rare for the standard jet clustering to produce two jets with less than this separation and our modification insures that it never happens.

B. Jet Corrections

The above procedure defines a jet as the energy in a cluster of towers within a particular radius. To obtain the parent-parton energy we must correct this energy for several effects: the energy response of the calorimeter, the energy deposited inside the 0.4 cone from sources other than the parent parton, and the parent-parton energy which radiates out of the 0.4 cone. These corrections are standard CDF jet correction procedures which are fully described elsewhere [14]. We also give brief descriptions of these corrections here.

The calorimeter energy response correction is designed to obtain an estimate of the true energy inside the clustering radius. This is achieved in two steps. First, the energy of jets in the plug and forward calorimeters are scaled to give the energy as it would be measured in the central calorimeter. The correction is derived from a sample of jet events containing one well-measured central jet opposite a second jet which can be anywhere in the detector. The relative jet function that is derived from this sample corrects the imbalance of the two jets as a function of the (measured) E_T and η of the second jet. After the jet energy is scaled to the central detector it is corrected for the response of the central detector. The result of these two steps is our best estimate of the true energy inside the 0.4 cone.

All energy inside the cone does not necessarily originate from the parent-parton. There are two contributions of cone energy contamination. First, underlying event energy from the spectator partons of the hard interaction is subtracted. The average contamination is 1.01 GeV. The second source of contamination is energy deposited into the cone from interactions other than the W boson interaction.

To obtain the contamination from interactions that occur in the same $\overline{p}p$ crossing as the W boson event we would like to have a sample selected from a completely unbiased trigger, alternatively known as a crossing trigger sample. A crossing trigger accepts all $\overline{p}p$ crossings as physics events and is representative of the extra interactions in W events since there is no significant selection bias for or against W events with extra interactions. The actual sample used to determine the contamination from extra interactions is a luminosity-weighted minimum-bias sample which is approximately a crossing trigger sample without the zero interaction events. We use a subset of the minimum-bias sample that is selected so that the distribution of instantaneous luminosity for all the events is well-matched to the distribution of instantaneous luminosity for our W events.

The energy in minimum-bias events is examined to see how much energy from these events would accidentally overlap with a jet cluster in a hard physics event. We employed a random cone method which checked calorimeter towers of minimum-bias events to determine the energy contained in a random cone of 0.4. The amount of energy was parameterized by the number of reconstructed vertices in the event. The average contamination of 0.4 cones was found to be 0.3 GeV for each vertex. This amount of energy is subtracted from each jet in the event for every vertex reconstructed in a W event except the W vertex (i.e. for every extra vertex). The uncertainty that we assign to the extra interaction energy and the underlying event energy is 50% as determined by a detailed examination of the random cone method.

The final correction to the jet increases the jet cone energy for energy that falls outside the 0.4 cone [15]. This out–of–cone correction accounts for energy that radiates from the parent parton at a large angle. The correction is parameterized by the jets transverse momentum because jets become narrower at large energies.

The combined corrections to the jets raise the measured jet energy by about 60% at $E_T = 15$ GeV (corrected energy). The error on the jet energy is 5.0% at $E_T = 15$ GeV. This value excludes the contribution to the error due to the uncertainty on the underlying event and extra interaction energy. These uncertainties contribute 3.3% additional error to the jet energy.

TABLE III. Event breakdown by jet multiplicities associated with W production. The number listed is the number of events with exactly the number of jets indicated rather than the inclusive (greater than or equal to) jet multiplicity.

Sample	N_W	Fraction
$W + 0$ jets	40287	0.7833
$W + 1$ jets	8548	0.1662
$W + 2$ jets	2016	0.0392
$W + 3$ jets	454	0.0088
$W + 4$ jets	105	0.0020
$W + 5$ jets	16	0.0003
$W + 6$ jets	5	0.0001
Total	51431	1.0000

C. Jet Counting

We count jets in W events using the following definition:

- jet $E_T \geq 15$ GeV
- jet $|\eta_{det}| \leq 2.4$.

The η_{det} requirement (2.4) is the jet η as measured from the center of the detector. This requirement limits us to the region of the calorimeter where the energy corrections are best understood. The jet transverse energy requirement is chosen to keep us in an energy region where the jet energy scale is well known. We find a total of 14472 jets in the W sample. The breakdown according to the number of jets in an event is give in Table III.

The error on the jet energy is the largest source of error in counting jets since the E_T distribution of jets is a steeply falling distribution (Figure 7). We present the error on the $W+$ jet cross section measurements due to the error on counting jets in section VII. The jet counting uncertainties are derived from the 5% jet E_T uncertainty, 3.3% underlying event and extra interaction uncertainty, and the $\pm$ 0.2 uncertainty on the jet η_{det}. The energy errors are with respect to a jet at E_T =15 GeV.

V. BACKGROUND CORRECTION TO W BOSON YIELDS

In section III we described the selection of $W \rightarrow e\nu$ events and in the previous section we defined a jet for the purposes of counting the number of jets in a W event. This section and the following will describe corrections to these raw numbers of $W+$ n jet candidates in order to obtain the production rates of direct single W's produced in association with n jets. Direct single W production refers to a single W produced from a $q\overline{q}$ annihilation as shown in Figure 1. Direct single W production dominates our $W+$ jet samples; however, other production processes will contribute a significant fraction of events to our samples.

The standard model predicts that the top quark will decay almost exclusively to a final state containing a W boson and a b quark. The final state of a top pair ($t\overline{t}$) decay in which one top decays to an $e\nu$ typically includes at least 2 jets and more likely 4 jets so that the contribution to our high multiplicity W samples is significant. Although top decay is a source of true W bosons we subtract its contribution from our data as a background in order to make comparisons with predictions for direct single W production.

True background events are those events which do not contain a $W \rightarrow e\nu$ decay yet leave a $W \rightarrow e\nu$ signature in the detector. The list of significant backgrounds is multijet events, $W \rightarrow \tau\nu$ and $Z \rightarrow e^+e^-$. The largest of these contaminations is multijet events which refers to direct QCD production of jets. These events have a small probability that the jet will produce an electron signature and that the event will simultaneously contain a large imbalance of transverse energy. However, since the production rate for multijets is much larger than W production even a small probability results in significant background rates. We use a sample of events enriched in QCD multijet events (created by loosening some of our selection criteria) to estimate the contribution from this background.

The remaining backgrounds from $W \rightarrow \tau\nu$ decay and $Z \rightarrow e^+e^-$ decay contribute a small but significant number of events to our W candidate samples. $W \rightarrow \tau\nu$ events are produced at the same rate as $W \rightarrow e\nu$ and 18% of the τ leptons decay to a final state electron. This background is efficiently rejected by the high transverse energy requirements on the electron and neutrino. These events will also have the same jet structure as $W \rightarrow e\nu$ events, so they will not alter our results. An electron from $Z \rightarrow e^+e^-$ decay passes our electron E_T requirement as easily as electrons from W decay so that we rely primarily on the $\not{E}_T$ requirement to reject these events. A $Z \rightarrow e^+e^-$ decay can achieve a large missing transverse energy if one of the leptons escapes the detector through an uninstrumented region. We use a detector simulation to obtain the fraction of $Z \rightarrow e^+e^-$ events for which one lepton passes the electron selection and the other escapes or is mis-measured enough to produce a large imbalance of transverse energy.

We subtract the backgrounds mentioned above from the total number of W events in our samples. We also correct for a special type of background which does not increase the total number of W's but does add to the number of jets in a W event. We refer to these backgrounds as *promotion* backgrounds because they promote a W event with n jets to a W event with $n+m$ jets. An example of a promotion is a jet produced by an extra interaction. Since we do not distinguish from which vertex a jet is produced we will count all jets as produced from the W interaction and correct our counts later. Although the probability for a promotion is very small the effect is enhanced by the fact that the higher jet multiplicity rates are being fed by the lower multiplicity channels which have much larger production rates.

A. Background from Top Quarks

1. Sources of Top Contribution

The $W+$ jet sample was used to establish the existence of the top quark at CDF [9], although the $W+$ jet sample used for the top analysis was not precisely the same as the sample used for this analysis. Both top and its antiparticle from top pair production will decay to a W boson and a b quark. The top discovery analyses achieved a sample enriched in top events by identifying the leptonic decays of W's and further enriching the sample for top by identifying events which contain b quarks. Although our W samples are not required to contain b quarks, the fraction of top events is expected to be significant in the subsamples with a high number of jets.

Since our W data selection requires an electron and neutrino, one of the W's from top pair decay is constrained to this decay mode. The other W can decay in any mode but it is the hadronic decay ($W \rightarrow q\overline{q'} \rightarrow$ hadrons) that introduces the largest contamination of our direct single W candidate sample. We refer to the mode in which the second W decays hadronically as the electron-jet mode. There are two reasons why the electron-jet mode produces the largest contamination. The branching ratio of the W to jets is 69% [16] and there are a total of 4 jets in this mode which places these events in the subsamples of the $W+$ jet events where the direct single W production rate is small. The calculation of the top background includes jet counting efficiencies as well the difference in the efficiency for finding W's produced from top. This is described in the next section.

2. Top Background Calculation

Our top contribution estimate is derived from a top Monte Carlo sample made by using the PYTHIA top event generator with all decay modes allowed and a top mass of 170 GeV/c^2 followed by a full detector simulation. First PYTHIA [17] generates and decays top pairs for 1.8 TeV $\overline{p}p$ collisions. The W bosons from the top decays are allowed to decay to any final state in order to obtain every possible background event.

The output from the generator is processed with a full detector simulation so that the efficiencies for finding W's and counting jets are modeled. A detector simulation also models the effect of a second electron or a τ faking a jet when the second W decays leptonically. The output from the detector simulation is in the same format as the data and we process the Monte Carlo events with the identical executable that is used to identify W events in our data sample.

There are 42000 top events generated (N_{gen}) for our calculation. Of these, 2596 events pass our W selection. The breakdown according to the number of jets reconstructed is presented in Table IV.

In order to extract a top expectation for our W analysis we must know the top mass, the top cross section at the mass of the top and the luminosity of our data sample. Because we are trying to compare the experimental results to QCD calculations, we have chosen to use the theoretical top cross section rather than the measured top cross section [18]. The top sample was generated at a mass of 170 GeV. The top mass measurement at CDF [19] yields a value of 176.0 ± 6.5 GeV/c^2. We correct our sample for the decrease in the cross section from a mass of 170 GeV/c^2 to 175 GeV/c^2. The luminosity of our top Monte Carlo is then calculated with

$$L_{gen} = \frac{N_{gen}}{\sigma_{t\overline{t}}\ (175)} = 7.6\ \mathrm{fb}^{-1} \tag{1}$$

This value is used to scale the numbers in Table IV to our data luminosity of 108 pb^{-1}. The expected top contribution as a function of the number of jets is presented in Table IV.

3. Top Background Systematic Error

The systematic error on our top background expectation includes the uncertainty of $t\overline{t}$ production rate due to the error on the luminosity of our W data sample (108 $\pm$ 9 pb^{-1}), the theoretical error on the top cross section ($\sigma_{t\overline{t}}$ (175) = 5.53 + .07 − .39 pb) [20] and the error on the top mass as measured at CDF. The top cross section at masses of 170.3 and 183.3 GeV/c^2 are 6.35 pb^{-1} and 4.61 pb^{-1} respectively. This variation dominates the systematic errors in Table IV.

TABLE IV. Results of top background calculation. The first column lists the number of $W+\geq n$ jet events selected from the 42000 top events generated. The second column gives the expected contribution to our data samples from top pair production and decay. The first error is statistical and the second is the systematic which is the sum of the top mass uncertainty, the luminosity uncertainty, and the theoretical uncertainty on the top cross section.

Sample	Number Selected	Background Expected
≥ 0 jets	2596	$36.9 \pm 0.7 \pm 7.3$
≥ 1 jets	2595	$36.9 \pm 0.7 \pm 7.3$
≥ 2 jets	2548	$36.2 \pm 0.7 \pm 7.2$
≥ 3 jets	2173	$30.9 \pm 0.6 \pm 6.1$
≥ 4 jets	1481	$21.0 \pm 0.5 \pm 4.2$

B. QCD Multi-Jet Background

1. Sources of QCD Multi-Jet Background

The backgrounds to $W \to e\nu$ come from any process which produces an electron-like energy deposition plus a large missing transverse energy. Multijet events, which we refer to as QCD background, can produce this signature if one jet leaves an electron signature in the detector and the transverse energy in the event is not well measured. In fact, QCD background is the largest source of background to the $W+$ jet events. Furthermore the rate is dependent on the number of jets so that systematic errors in the background estimates do not completely cancel in the relative $W+\ n$ jet cross sections which we use to determine the absolute cross sections. To keep the error on our cross section due to background subtraction comparable to the statistical uncertainty of our $W+\ n \geq$ 4 jet sample, we need to know the QCD background to $\approx 35\%$.

Our identification of a W electron includes the use of both tracking and calorimetry information. To fake a W electron, a jet in a multijet event must leave a high P_T track in the CTC in addition to an electromagnetic energy deposition associated with this track. This dual tracking-calorimeter signature can be produced from hadron jets through several modes. Heavy flavor jets where charm or bottom quarks decay to real electrons can leave an electron signature in the detector. Gammas, converting to electron positron pairs, are a source of W background. Also included in the conversion electron sources are Dalitz pairs. Finally, π^0- $\pi^{\pm}$ overlaps and hadronic jets which shower early in the calorimeter can leave a well-isolated EM energy deposit with associated tracks.

In addition to producing an electron signal, the multijet background event must have a large missing transverse energy. Large missing transverse energy in a multijet event can be attributed to the escape of significant energy from of one or more jets through uninstrumented regions between the detectors that results in the mismeasurement of the jet.

2. Datasets for QCD Background Calculation

In order to obtain the QCD background we need to define a sample of events enriched in QCD multijets. In our selection of W events we used the electron isolation variable (section III A 2) to discriminate between electrons and jets. We also rejected a large amount of QCD background by requiring a large imbalance of transverse energy. Therefore to obtain a sample of QCD multijet events we remove these requirements from our W selection. Specifically, we select a QCD sample with the following criteria

- Apply all W selection requirements except:
  - Iso(0.4) ≤ 0.1
  - $\not\!\!E_T \geq 30$ GeV.

This sample contains 214046 events. Of course the W candidates are in this sample but they will be confined to one corner of the isolation-$\not\!\!E_T$ plane. A lego plot of isolation versus $\not\!\!E_T$ is shown in Figure 8. From this figure we can easily distinguish the regions which are mostly W boson events (low isolation, high $\not\!\!E_T$) and mostly multijet events (everywhere else). The estimate of the QCD background will extrapolate from the multijet dominated regions to the W dominated regions.

Removing the isolation and $\not\!\!E_T$ requirements in the data selection also invites some contamination from electroweak processes such as $Z \rightarrow e^+e^-$ and $W \rightarrow \tau\nu$ events. These will concentrate in the low isolation and low $\not\!\!E_T$ region of the isolation-$\not\!\!E_T$ plane. We employ a set of requirements to reject the electroweak contamination of these regions.

We remove $Z \rightarrow e^+e^-$ and Drell-Yan contamination by vetoing events with a second electron regardless of the mass of the electron-positron pair. However, if a second electron exists and is within a radius of 0.4 of the first electron the isolation of the two are correlated resulting in poor isolation of both electrons. The isolation of the first electron versus the second electron is shown in Figure 9 for the QCD sample before any electroweak contamination is removed.

If the e^+e^- pairs are close enough each appears in the isolation definition of the other. These events rarely allow the isolation of the first electron to pass our W selection; however, the spoiled isolation of the first electron also results in the failure of the e^+e^- removal requirements. Since these events do not contribute to W + jets yet do appear in the multijet background sample we must explicitly remove them from our multijet sample.

To enrich the sample further in multijet events we require that there is at least one other high energy cluster (besides the selected electron). The fraction of electromagnetic energy in this jet must be less than 0.8. This last selection criteria for a second energy cluster is only applied to the low $\not\!\!E_T$ events (regions a and b) where we expect all jets were measured reasonably well and therefore expect at least two high E_T jets.

3. Measurement of QCD Background

In order to estimate the amount of QCD background in the W sample, we make the assumption that the electron's isolation is independent of the $\not\!\!E_T$. The first step in estimating the QCD background is to divide our QCD sample into 4 subsamples which are defined by their position in the isolation-$\not\!\!E_T$ plane (Figure 8). We label the regions a,b,c and d.

region a: $Iso < 0.1$; $\not\!\!E_T < 10$
region b: $Iso > 0.3$; $\not\!\!E_T < 10$
region c: $Iso > 0.3$; $\not\!\!E_T > 30$
region d: $Iso < 0.1$; $\not\!\!E_T > 30$

From the definitions of the regions above one sees that we have excluded intermediate regions from consideration. This exclusion is to insure that regions a, b and c are pure multijet and not a mix of QCD and W events. We exclude events with an electron isolation in the region 0.1 to 0.3 and any events with a $\not\!\!E_T$ in the region 10 to 30 GeV. This requirement rejects $W \rightarrow e\nu$ leakage as well as $W \rightarrow \tau\nu$ events which have an average $\not\!\!E_T$ less than $W \rightarrow e\nu$ events but generally larger than 10 GeV.

A first order description of the isolation extrapolation method assumes the isolation shape for QCD jets faking electrons is independent of $\not\!\!E_T$ of the sample (see Figure 10). Therefore, if the ratio ($\frac{N_a}{N_b}$) of well-isolated to poorly-isolated QCD events is known for the low $\not\!\!E_T$ region then it is known in the high $\not\!\!E_T$ region. We directly count the number of multijet events (N_c) with poor isolation and large $\not\!\!E_T$. With these quantities the number of QCD background events in the W sample ($N_{\rm QCD}$) is

$$N_{\rm QCD} = \frac{N_a}{N_b} \cdot N_c. \qquad (2)$$

4. Tests of the QCD Background Calculation

The large statistics of the Run 1 data sample allow direct tests of the isolation extrapolation method. For these tests we select two subsamples of the QCD sample, which is the superset of our selected W events made by removing the isolation cut and the $\not{E}_T$ cut. The low $\not{E}_T$ sample consists of all events with a $\not{E}_T$ less than 10 GeV. The anti-isolated sample is defined by an electron isolation greater than 0.3. These two samples which are shown in Figure 11 contain essentially no W events. To test the isolation extrapolation method we divide each of these samples into four regions just as we did with the QCD superset of events. Within each sample we can calculate the events in the new region d from the other three regions. We can also directly count the events since these are no longer dominated by W events. The calculations and observations are compared directly in Table V.

Overall, Table V shows the method performs with the desired accuracy (35%). We use the test from the anti-isolation sample to assign a systematic of 30% to the QCD background calculation at each multiplicity.

TABLE V. Results for the tests of the QCD background calculation. The predicted number of events in region d and the observed number of events are compared. The first column lists the results for the low $\not{E}_T$ sample and the second column lists the results for the poor isolation sample. Both samples are essentially free of W contamination.

	Low $\not{E}_T$ Sample $\not{E}_T \leq$ 10 GeV		Anti-isolation sample Isolation $\geq$ 0.3	
	Predicted	Observed	Predicted	Observed
$\geq$ 0 jets	16522	15399	301	235
$\geq$ 1 jets	13658	12480	263	198
$\geq$ 2 jets	2782	2724	101	97
$\geq$ 3 jets	569	543	29	29
$\geq$ 4 jets	105	93	8.5	10

5. *QCD Background Results*

The calculated QCD backgrounds are listed in Table VI. We see that the QCD contamination is significant and that the probability of contamination from multijet events increases with the number of jets in the $W+$ jet samples.

C. Single Boson Background

1. *Sources of Single Boson Background*

W decay in which a final state electron results from an intermediate particle such as the τ can contribute to our $W \rightarrow e\nu$ + jet samples. $W \rightarrow \tau\nu$ accounts for one third of the leptonic W decays and the τ has a significant branching fraction (18%) to electrons. These events will sometimes be identified as $W \rightarrow e\nu$ decay. However, the momentum of the τ is shared among three decay products ($e\nu\nu$), two of which do not deposit energy in the calorimeter. Our kinematic requirements reject most of the $W \rightarrow \tau\nu$ events.

TABLE VI. Final results for QCD background. The first column is the number of W events selected with at least n jets. The second column presents the expected contamination of the W sample from QCD background. The first uncertainty is the statistical error and the second is systematic uncertainty.

	W Candidates	QCD Background
$\geq$ 0 jets	51431	1509 $\pm$ 73 $\pm$ 453
$\geq$ 1 jets	11144	1248 $\pm$ 65 $\pm$ 374
$\geq$ 2 jets	2596	412 $\pm$ 31 $\pm$ 124
$\geq$ 3 jets	580	125 $\pm$ 17 $\pm$ 38
$\geq$ 4 jets	126	33.6 $\pm$ 8.1 $\pm$ 10.0

An accurate estimate of the $W \rightarrow \tau\nu$ + jet contamination of our $W \rightarrow e\nu$ + jet samples is made using a LO QCD calculation for $W \rightarrow \tau\nu$ + jets events. The QCD production diagrams are the same whether the W decays to an electron or τ final state. We use this fact to remove the renormalization scale dependence inherent in LO QCD predictions. Rather than extracting an absolute prediction of the $W \rightarrow \tau\nu + \geq n$ jet cross section, we extract the ratio

$$R_{W \rightarrow \tau\nu} = \frac{\sigma(W \rightarrow \tau\nu\ ) \cdot \epsilon(W \rightarrow \tau\nu\ )}{\sigma(W \rightarrow e\nu\ ) \cdot \epsilon(W \rightarrow e\nu\ )}. \tag{3}$$

The ϵ in equation 3 is the efficiency for finding a W boson which is dependent on the decay mode. The ratio as calculated from equation 3 used with the counts in our W + jet data samples yields $W \rightarrow \tau\nu$ background.

Another significant source of high E_T electrons is produced from $Z \rightarrow e^+e^-$ decays. The electron E_T spectrum is similar to that of electrons from $W \rightarrow e\nu$ but the Z cross section is a factor 10 below that of the W cross section. Although we have explicitly removed $Z \rightarrow e^+e^-$ decays from the W sample (section III C) the efficiency for our $Z \rightarrow e^+e^-$ identification was about 50%. A fraction of the Z's that failed the Z selection will contribute to our W events. If one lepton in the Z decay passes the electron selection and the other escapes through a gap in the detector coverage then a W signature can result. The calculation we use to estimate the rate of $Z \rightarrow e^+e^-$ events faking $W \rightarrow e\nu$ is identical to the $W \rightarrow \tau\nu$ method described above.

2. *Single Boson Background Samples and Results*

We generate leading order $W \rightarrow \tau\nu + \geq n$ jet Monte Carlo samples using VECBOS. The renormalization scale is $Q^2_{ren} = M^2_W$. We use HERWIG to add initial/final state radiation and provide fragmentation of the partons with the HERWIG fragmentation scale (Q^2_{frg}) set equal to $M^2_W + P^2_t$. The program (TAUOLA [21]) used to decay the τ allows all final states and provides the correct polarization. The Monte Carlo events are processed through the CDF detector simulation code (QFL) and our W selection executable is used to select events with the identical requirements used for data selection. A description of the Monte Carlo generation is found in section VIII.

For each $W \to \tau\nu + \geq n$ jet sample we create a $W \to e\nu + \geq n$ jet sample with identical generation parameters. The ratio in equation 3 is determined by the number of events passing our W selection requirements from both the $W \to \tau\nu$ and $W \to e\nu$ Monte Carlo samples. We use the following formulas to determine the backgrounds:

$$N_{W \to \tau\nu} = R_{W \to \tau\nu} \cdot N_{W \to e\nu} \tag{4}$$

$$N_{Z \to e^+e^-} = R_{Z \to e^+e^-} \cdot N_{W \to e\nu} \tag{5}$$

where

$$N_{W \to e\nu} = \frac{N_{Selected} - N_{QCD} - N_{top}}{(1 + R_{W \to \tau\nu} + R_{Z \to e^+e^-})} \tag{6}$$

and

$$R_{Z \to e^+e^-} = \frac{\sigma(Z \to e^+e^-) \cdot \epsilon(Z \to e^+e^-)}{\sigma(W \to e\nu) \cdot \epsilon(W \to e\nu)}. \tag{7}$$

These equations assume that no other contamination besides QCD and top exist in the W data. The results are shown in Table VII for $n = 1$ through 4. The results show that the contaminations from $W \to e\nu$ and $Z \to e^+e^-$ are small and will have a negligible effect on the relative cross section measurements. The asterisk identifies samples for which the calculation could not be performed because the LO generator was not available. We extrapolated assuming a flat behavior. This extrapolation should be safe given the background is fairly insensitive to the number of jets but we have increased the error for these extrapolations by a factor 2.0.

TABLE VII. Expected background for $W \to \tau\nu$ and $Z \to e^+e^-$. Fractions are number of background over number of $W \to e\nu$. The asterisk identifies samples for which an extrapolation based upon flat behavior is used because the calculation could not be performed.

	$W \to \tau\nu$		$Z \to e^+e^-$	
Sample	fraction	background	fraction	background
≥ 0 jets	0.0150	726	0.0155	752(*)
≥ 1 jets	0.0217	196	0.0173	157
≥ 2 jets	0.0329	62.9	0.0137	26.3
≥ 3 jets	0.0213	7.87	0.0155	5.73
≥ 4 jets	0.0213	1.26(*)	0.0155	0.92(*)

D. Multiplicity Promotion Background

1. Sources of Multiplicity Promotions

The previous sections discussed contributions to the W candidates selected for our $W+$ jet analysis. Here we discuss backgrounds which do not contribute to the total number of W events but rather add to the number of jets in a W boson event. We correct for two contributions of jets which do not arise from direct single $W+$ jet production:

- jets produced in interactions that occur in the same crossing as the W interaction; and
- γ's in $W\gamma$ events which are counted as jets.

About 40% of our W events have at least one other vertex reconstructed in addition to the W boson vertex. The extra vertices indicate the presence of additional $\overline{p}p$ interactions, although some low-multiplicity interactions do not make a vertex that passes our vertex selection criterea. Typically these extra interactions contribute a small amount of energy which is spread over the detector. As we discussed in section IV B this energy is subtracted from our jet energy with a value determined by the number of extra vertices that we find in the W event. Occasionally the energy from an extra interaction will be large enough and localized enough to result in a reconstructed jet. These jets will be counted along with any jets produced in association with the W boson, so we correct the jet multiplicity distributions to account for these extra jets.

2. Calculation of Promotions

The probability of a W event containing a jet that is generated from an extra interaction is 0.0099. This value was calculated from our minimum-bias events (see section IV B for the definition of this sample). The events in the minimum-bias sample closely model the extra interactions found in W events. Specifically, neither sample has a significant bias in triggering its acceptance. This is true for minimum-bias samples by design.

We counted the number of jets and the number of vertices in our minimum-bias sample. Note that the number of vertices is different from the number of interactions because not every interaction will produce an identified vertex, and multiple interactions very close together cannot be separated into multiple vertices. However, the number of vertices per interaction should be the same for the minimum-bias sample and the extra interactions in the $W+$ jets sample.

We found that for every 81 vertices in the minimum-bias sample, one single-jet event was found. The W sample contains 41188 vertices in addition to those vertices associated with the W bosons. We then expect 507 events with a single extra jet from an extra interaction in our W sample. This number of jets in 51431 W events yields the probability of 0.0099 for obtaining a single jet from an extra interaction per W event. The formula is shown explicitly in equation 8 below. In equation 8, $N_{\rm jet}(\rm MB)$ is the number of jets in the minimum-bias sample, $N_{\rm vtx}(\rm MB)$ is the number of vertices in the minimum-bias sample, $N_{\rm extra\ vtx}(W)$ is the number of extra vertices found in the W sample, and P_1 is the probability for a jet to arise from an extra interaction in a W event. The calculation is repeated for the probability of obtaining 2, 3, and 4 jets from an extra interaction by using the number of minimum bias events with 2, 3, and 4 jets, respectively. The probabilities are listed in Table VIII and are seen to drop by a factor 6 with the addition of each additional extra jet.

$$P_1 = \frac{N_{\rm extra\ vtx}(W)}{51431} \cdot \frac{N_{\rm jet}(\rm MB)}{N_{\rm vtx}(\rm MB)} \tag{8}$$

Despite the fact that the probability for obtaining a jet from an extra interaction is less than a percent, the correction for multiplicity promotions can be significant. The 1% of $W+$ 1 jet events which get promoted to $W+$ 2 jet events represent a 5% increase on the number of $W+$ 2 jet sample because the 2 jet sample is roughly 5 times smaller. The $W+$ 2 jet sample is also increased by promotions from the $W+0$ jet sample. The probability of a 2-jet promotion is 6 times smaller but the $W+$ 0 jet sample is 5 times larger than the $W+$ 1 jet sample. This means that the correction to the $W+$ 2 jet sample for $W+$ 0 jet promotions is roughly the same as that for $W+$ 1 jet promotions. The effect of the promotions therefore represents our second largest background correction to the $W+$ jet samples (except at some higher jet multiplicities where top event background becomes significant).

A second source of promotion arises from $W\gamma$ events. The photon in these events will be counted as a jet if its transverse energy is above 15 GeV and $|\eta|$ is less than 2.4.

The probability (P_γ) that a photon will contribute a jet to an event in our W sample is 0.004 ± 0.0006. This value was determined from $W\gamma$ Monte Carlo events. We corrected the photon energy using the standard jet corrections. These corrections are necessary since we do not distinguish photons and jets in the data. After obtaining the number of photons which pass the jet selection requirements in the Monte Carlo, we scale the Monte Carlo luminosity to our data luminosity. We expect 207 ± 32 photons measured as jets in the W sample. This number of photon-jets yields the value of P_γ (207/51431).

TABLE VIII. The table shows the number of events found with m jets in the minimum bias sample and the probabilities for obtaining a single jet, 2 jets, 3 jets and 4 jets from an extra interaction. We use the number of vertices (40117) found in the minimum-bias sample and the number of extra vertices (41188) found in the W sample to calculate the probabilities in the second column (equation 8).

m jets	N Events	P_m
1 jet	494	9.9×10^{-3}
2 jets	67	1.3×10^{-3}
3 jets	11	2.2×10^{-4}
4 jets	2	4.0×10^{-5}

To correct for photons faking jets we add P_γ for a photon faking a jet to the probability (P_1) of obtaining 1 jet from an extra interaction.

The actual correction for promotions is complicated by the fact that we must simultaneously correct for the jets being promoted to and from a particular jet multiplicity. In the promotion calculation we use a matrix of probabilities which maps the n jet sample to the $n+m$ jet sample via the promotion probability for m jets from extra interactions. The corrections to the $W+\geq n$ jet samples are shown in Table IX and are calculated for m as high as 4.

TABLE IX. Summary of backgrounds to single $W+\geq$ jet samples.

Background	≥ 0 jets	≥ 1 jet	≥ 2 jets	≥ 3 jets	≥ 4 jets
QCD	1509	1248	412	125	33.6
$W \to \tau\nu$	726	196	62.9	7.87	1.26
$Z \to e^+e^-$	752	157	26.3	5.73	0.92
Top	36.9	36.9	36.2	30.9	21.0
Promotion	0	464	149	40.8	9.92

3. Uncertainty on the Promotion Correction

Although the most reliable method for obtaining the promotion probabilities (P_m) is from the minimum-bias sample as described in the preceding section, we have estimated the number of jets from extra interactions in the W events from other methods to establish an error.

One study looked at the $\Delta\phi_{ej}$ distribution between the electron and jet in $W+$ jet events. The electron from W decay is uncorrelated with jets from an independent interaction therefore this distribution is flat. The distribution for jets produced in association with W bosons will be peaked at π. The actual $W+$ jet data was fit with these distributions to extract the amount of each.

Another study divided the $W+$ jet sample into 4 subsamples dependent on the average instantaneous luminosity at which the events were collected. We would expect that in high luminosity running the average number of extra interactions that occur would increase. This increase would result in a higher probability for jets from extra interactions.

The two studies gave results which bracketed our estimate from the minimum-bias sample and from these we quote an error on the promotion probabilities of +100% and -50%.

VI. EFFICIENCY CORRECTION TO W BOSON YIELDS

We restrict electrons to be in the region of the detector where the most reliable electron measurements are made. This requirement necessarily involves the loss of a large fraction of the W's produced at CDF. In this section we determine our losses from this requirement and all other requirements made in our W data selection. Since some W selection requirements are biased against events with jets, we measure the efficiency for each $W+$ n jet sample independently. The total efficiency for each W sample is the product of all individual efficiencies as shown in equation 9. The descriptions of these efficiencies are in Table X.

$$\epsilon_{tot} = \epsilon_{geo} \cdot \epsilon_{kin} \cdot \epsilon_{ID} \cdot \epsilon_{trig} \cdot \epsilon_{obl} \cdot \epsilon_{Zrem} \tag{9}$$

TABLE X. Efficiencies related to losses to the $W \to e\nu$ sample due to the selection criteria.

Name	description
Geometric(ϵ_{geo})	electron in central detector
	electron in well-instrumented region
Kinematic(ϵ_{kin})	electron $E_T \geq 20$ GeV
	$\not\!\!E_T \geq 30$ GeV
Identification(ϵ_{ID})	passes event and electron quality cuts
Trigger(ϵ_{trig})	passes online trigger requirements
Obliteration(ϵ_{obl})	loss of events due to electron-jet overlap
Z removal(ϵ_{Zrem})	loss of $W+$ jet events due to Z removal

A. Geometric and Kinematic Acceptances

1. Acceptance Calculation for W $+ \geq n$ Jets

The efficiency for geometric and kinematic restrictions on the leptons is referred to as the acceptance. The geometric and kinematic acceptances are calculated separately. The geometric acceptance is the fraction of electrons that deposit energy in a fiducial region of the central electromagnetic calorimeter. The kinematic acceptance is the fraction of electrons and neutrinos to pass the E_T and $\not\!\!E_T$ requirements respectively. The fractions are calculated with simulated $W \to e\nu$ events.

2. $W+$ Jet Monte Carlo Samples

We generate W + n parton data samples using the VECtor BOSon leading order Monte Carlo generator VECBOS [22]. VECBOS includes the correlations between the vector boson decay fermions and the rest of the event. The renormalization (Q^2_{ren}) scale for the calculation is the average parton P_T squared ($< P_T >^2$). The generator output consists of the four-momenta of the final state partons, and we apply the following requirements at the parton level to avoid divergences and to confine partons to the detector acceptance:

- parton $E_T \geq 8.0$ GeV;
- parton $|\eta| < 3.5$; and
- parton separation $\Delta R \geq 0.4$.

No requirements are imposed upon the leptons from the W decay.

The evolution of the parton level hard scattering process into hadrons is carried out using HERWIG [23], which includes initial state gluon radiation from the incident partons as well as color coherence in the final state radiation. The cutoff on the virtuality limit of the emitted gluons in HERWIG is $Q^2_{frg} = M^2_W + P^2_{TW}$. Further details of the Monte Carlo parton generation and fragmentation are discussed in section VIII.

The Monte Carlo events are passed through the CDF detector simulation (QFL) to obtain the energy measured by the detector for electrons, jets, and the underlying event. The simulated events are processed by the same analysis code used for the data; events selection requirements and jet counting criterea are identical to those used for real events. For consistency in the modeling of our W events, the W plus 0 jets sample is generated with VECBOS using a parton P_T requirement lowered to 1 GeV but with the Monte Carlo W P_T distribution tuned off the real W data.

3. Geometric Acceptance

We require the electron to be in the central region of the detector ($|\eta| \leq 1.1$). The region of the electron is determined from the reconstructed electron rather than the four-vector from the matrix element calculation so that we include detector smearing. The second acceptance requirement applied to the electron is the fiducial requirement. Good fiducial status requires the electron

TABLE XI. Number of events passing each acceptance requirement for our 0 to 4 jets samples.

Sample	N	$N_{central}$	$N_{fiducial}$	N_{E_T}	$N_{\not{E}_T}$
$W+0$ jets	42836	23699	17863	15238	10054
$W+1$ jets	37282	21486	16290	14139	8955
$W+2$ jets	10972	6543	4954	4305	2647
$W+3$ jets	3848	2383	1819	1566	1053
$W+4$ jets	1399	873	654	575	384

to be in a well-instrumented region of the calorimeter. The number of events with a central fiducial electron as a function of the jet multiplicity is shown in Table XI.

In a small percentage of events the electron is not reconstructed. We determine the cause of such losses by using the four-vector from the matrix element calculation and propagating the electron into the detector. These "lost" electrons fall into two classes: electrons which escape the detector and electrons which are obliterated. An obliterated electron is defined as an electron which overlaps with a jet to the extent that electron reconstruction fails. The rate of obliteration is measured separately (section VI D) using data. After propagating the electron the acceptance status is properly categorized. Table XII lists the geometric acceptance for our W + jets samples.

4. Kinematic Acceptance

We apply a 20 GeV transverse energy requirement to electrons in events which pass the geometry requirements. The electron energy is corrected with the Monte Carlo electron correction code which is the equivalent of the corrections used on W data events. The number of events surviving the electron E_T requirement are presented in Table XI.

Events with an electron $E_T \geq 20$ were tested for a $\not{E}_T \geq$ 30 GeV. We calculate the imbalance of transverse energy from fully corrected detector energy and include the effects of extra interactions.

5. Acceptance Summary

Our measured W acceptances are shown in Table XII. The results are given for exclusive jet multiplicities with n=0 to 4. The measurement used a LO matrix element calculation with partial higher order corrections via a HERWIG parton shower simulation. The detector simulation QFL was used to model the response to electrons and the recoil to the W.

TABLE XII. Geometric and kinematic acceptances for W + jets. The last column shows the total acceptance with the statistical error and the systematic error respectively. The systematic uncertainty comes from varying the jet energy scale as described in Section VI G, which has no effect on the 0 jet sample.

Sample	Geometric	Kinematic	Total
$W+0$ jets	0.4170	0.5629	0.2347 $\pm$ 0.0020
$W+1$ jets	0.4369	0.5497	0.2402 $\pm$ 0.0022 $\pm$ 0.0021
$W+2$ jets	0.4515	0.5342	0.2412 $\pm$ 0.0041 $\pm$ 0.0025
$W+3$ jets	0.4727	0.5791	0.2737 $\pm$ 0.0072 $\pm$ 0.0045
$W+4$ jets	0.4675	0.5877	0.2747 $\pm$ 0.0119 $\pm$ 0.0100

B. ID Efficiency

We showed in section III A that an effective means of selecting electrons while reducing backgrounds was to impose electron quality criteria on the electromagnetic cluster in the central calorimeter. This procedure necessarily involves the loss of true electrons that happen to fail these requirements. Simulations of electron response are difficult because some of these requirements are sensitive to the running conditions such as the luminosity while others could show time dependent behavior due to the slow degradation of detectors such as the calorimeter. An example of the former is the isolation variable. As the luminosity increases the average number of interactions increases. The contamination of the electron energy by extra interactions increases with the number of interactions and therefore with the luminosity. To obtain reliable efficiency numbers we measure the efficiency using data rather than simulations. The Z data is a very suitable sample for several reasons: The Z data were collected over the same time period as our $W+$ jet data; The kinematics of Z and W boson decay are similar; and Z bosons are easily found and contain very small backgrounds.

1. The ID Efficiency Sample and Calculation

The event sample used for determining ID efficiencies is derived from the inclusive electron sample by selecting events that have at least one lepton which passes our tight electron selection requirements. From this sample we apply the following requirements to a second electron:

- central ($|\eta| \leq 1.1$);
- $E_T \geq$ 20 GeV; and
- in the fiducial region.

The result is a sample where both leptons are central and fiducial and both have a $E_T \geq 20$ GeV. The following

TABLE XIII. ID efficiency for electrons as a function of the number of jets.

Sample	N_P	N_{PP}	ϵ_{ID}
$=0$ jets	2128	1690	0.885 ± 0.005
$=1$ jets	439	348	0.884 ± 0.012
$=2$ jets	107	83	0.874 ± 0.026
$=3$ jets	18	14	0.875 ± 0.062
≥ 4 jets	4	3	0.857 ± 0.141

TABLE XIV. Trigger efficiency for electrons as a function of the number of jets.

Sample	ϵ_{trig}
$=0$ jets	0.9936 ± 0.0005
$=1$ jets	0.9969 ± 0.0007
$=2$ jets	0.9947 ± 0.0022
$=3$ jets	0.9959 ± 0.0041
≥ 4 jets	0.9667 ± 0.0232

additional event requirements are made to insure that we have clean Z bosons:

- $Q_{e^+} + Q_{e^-} = 0$;
- $81 \leq M_{e^+e^-} \leq 101$; and
- $|Z_{vtx}| \leq 60.0$ cm.

There are 2696 events which satisfy these requirements ($\equiv N_P$). In 2138 of these events both the electron and positron pass the electron quality requirements ($\equiv N_{PP}$).

We have assumed that our ID efficiency calculation is independent of the number of jets in the event. We did this because we calculated the efficiency with obvious jet dependence separately (see section VI D. To check that this was a reasonable course of action we recalculate the ID efficiency for each $Z+$ jet sample. The results are shown in Table XIII. We do not observe a significant trend for the efficiency as a function of jet multiplicity so we use the single combined number in the calculations.

C. Trigger Efficiency

All events in our data sample must pass the level-two and level-three inclusive central electron triggers. To determine the fraction of electrons which fail these triggers we select a new W boson sample from the $\not\!\!E_T$ triggers at level-two and level-three which are based on identifying neutrino candidates instead of electron candidates. This trigger provides a dataset from which to select W bosons without the requirement of an electron trigger. From these events we select W events by applying our geometric, kinematic and extra tight electron selection (limiting the isolation to less than 0.05 to effectively eliminate multijet background). The $\not\!\!E_T$ is required to be at least 25 GeV. We check that the electron from these events passes the level-two and level-three central electron triggers. We find that trigger efficiency is 0.9941 ± 0.0004. The results are presented as a function of the number of jets in Table XIV and show no dependence with jet multiplicity so we use the single combined number in the calculations.

D. Electron-Jet Overlap Losses

In this section we factor out the losses that depend on the jet activity in the event. As part of the W selection we require that the electron and any high E_T jets be separated by a ΔR of no less than 0.52. We can only apply this requirement when we can physically distinguish an electron from a jet. If a jet and an electron occupy the same area of the detector we might lose the electron altogether. These events by their nature will not appear in the electron data samples therefore we need to simulate the effect from existing data. We refer to the efficency for events to appear in the electron data samples and to have ΔR to the nearest jet no less than 0.52 as the obliteration efficency.

1. Electron-Jet Overlap Data Samples and Calculation

We estimate the rate at which jets and electrons overlap from Z data events. We remove the Z boson decay products from the event and then use a Monte Carlo to decay W or Z bosons with the same momentum as the original Z boson. We decay a boson many times and observe the rate that the electron from the decay falls on top of a jet in the event. The advantage of the Z data is that it contains all sources of low-energy hadronic contamination of the electron. The disadvantage of the Z data is the limited statistics for events with high jet multiplicity. Although we decay the Z events several thousand times, systematic effects can enter the calculation because of the limited number of events. We are unable to use our much larger W sample for this estimate because the longitudinal momentum of the W is unknown.

We check to see if the electron from boson decay lands near any jets in the event. The criteria for the electron to be obliterated by jet activity is the following:

- a jet cluster with an $E_T(\text{jet}) \geq 0.1 \cdot E_T(ele)$ within a cone of 0.4 of the electron cluster; and
- a jet satisfying our jet selection criteria ($E_T \geq 15$ GeV and $|\eta| \leq 2.4$) within a cone of 0.52 of the electron.

TABLE XV. Electron-Jet obliteration Efficiency for W + jets Monte Carlo, and for this efficiency scaled to the low-jet-multiplicity Z data. Only the ratio of the efficiency to the 0-jet value enters into the cross section calculations.

Sample	ϵ_{obl}	ϵ_{obl} (scaled)
$=0$ jets	0.956 $\pm$ 0.010	0.948 $\pm$ 0.010
$=1$ jets	0.924 $\pm$ 0.009	0.917 $\pm$ 0.009
$=2$ jets	0.894 $\pm$ 0.011	0.887 $\pm$ 0.011
$=3$ jets	0.863 $\pm$ 0.009	0.856 $\pm$ 0.009
≥ 4 jets	0.826 $\pm$ 0.012	0.819 $\pm$ 0.012

Our final results of decaying the W and Z bosons are shown in Figure 12. This plot shows the fraction of events which pass our electron-jet obliteration criteria. The errors are obtained by varying the polarization of the boson. The quantity that enters the W cross section calculations is the ratio of the efficiencies for the different jet multiplicities and not the absolute magnitude of the efficiency. Where the Z statistics allow comparison, this ratio agrees for the Z and W samples. The magnitude of the obliteration efficiency indicates that the W Monte Carlo is a little more efficient than the Z data (Figure 12). This is not surprising since low-energy contamination is not modeled well by the Monte Carlo, and this could cause some additional loss in the data. Since the ratio is estimated better for high jet multiplicities from the Monte Carlo, we use these in our cross section calculation. The values for the electron-jet obliteration efficiency are shown in Table XV. Also shown in this Table are the Monte Carlo efficiencies scaled to match the low-multiplicity efficiencies estimated from the Z data. These scaled efficiencies represent our best estimate of the true values.

E. Z Removal

Our selection of W events includes a rejection of events which pass loose Z identification requirements (section III C). These requirements are applied to a second electron after the primary electron identification and $\not\!\!E_T$ requirement. This procedure is repeated on the W Monte Carlo. Although the Monte Carlo sample is entirely W + jets events, some jets in these events look enough like a second electron so that the event passes Z identification. Therefore the fraction of W events that pass the Z identification is dependent on the number of jets. Table XVI shows the efficiency for Z removal as calculated from our W Monte Carlo.

TABLE XVI. Z removal efficiency for W + jets.

Sample	Z removal
$W+0$ jets	1.0000 $\pm$ 0.0
$W+1$ jets	0.9976 $\pm$ 0.0005
$W+2$ jets	0.9953 $\pm$ 0.0014
$W+3$ jets	0.9881 $\pm$ 0.0035
$W+4$ jets	0.9846 $\pm$ 0.0062

TABLE XVII. Summary of W+ jet efficiencies.

Eff	$=0$ jets	$=1$ jets	$=2$ jets	$=3$ jets	$\geq$4 jets
ϵ_{geo}	0.4170	0.4369	0.4515	0.4727	0.4675
ϵ_{kin}	0.5629	0.5497	0.5342	0.5791	0.5877
ϵ_{ID}	0.8846	0.8846	0.8846	0.8846	0.8846
ϵ_{Trig}	0.9941	0.9941	0.9941	0.9941	0.9941
ϵ_{obl}	0.9478	0.9172	0.8867	0.8561	0.8192
ϵ_{Zrem}	1.0000	0.9976	0.9953	0.9881	0.9846
ϵ_{tot}	0.1956	0.1933	0.1872	0.2036	0.1948

F. Summary of Efficiencies

We have measured the efficiencies for identifying $W \rightarrow e\nu$ decays as a function of the number of jets. The individual and total efficiencies are collected in Table XVII. One source of W boson loss has not been determined in these estimates. The loss of a $W \rightarrow e\nu$ events due to our requirement that the event vertex is within 60 cm of the center of the detector is not dependent on the number of jets and therefore will cancel in our final cross section measurements since we scale our cross section to a previous CDF inclusive W measurement. The value has been determined for the Run 1a data to be $(95.55 \pm 1.05)\%$ and $(93.7 \pm 1.1)\%$ for Run 1b.

G. Systematic Uncertainties

In this section we present the systematics which can change the ratio of the acceptance of $W + n$ jets to that of $W + 0$ jets. We recalculate the acceptance from the CDF simulation program QFL after shifting the jet energy scale by +/− 5.0%. This scaling will not only affect jet counting but will change the measurement of the $\not\!\!E_T$ which depends on the measurement of jet energy. The absolute shifts of the acceptance for this procedure are shown in Table XVIII. We also have a choice for the renormalization scale when generating $W + n$ jets Monte Carlo. We expect some dependence on this parameter since the acceptance does depend on P_T and a $Q^2 = M_W^2 + P_{TW}^2$ would yield a harder P_T spectrum than our

TABLE XVIII. Acceptances for variations in renormalization scale and jet energy scale.

Sample	Default	$Q^2_{ren} = P^2_{TW} + M^2_W$	+5% Et Scale	-5% Et Scale
$W+1$ jets	0.2402	0.2406	0.2420	0.2381
$W+2$ jets	0.2412	0.2423	0.2434	0.2407
$W+3$ jets	0.2737	0.2766	0.2729	0.2702
$W+4$ jets	0.2747	0.2756	0.2847	0.2717

default choice of $Q^2 =< P_T >^2$ (parton P_T). The shifts due to a change in the renormalization scale are also presented in Table XVIII.

VII. DATA RESULTS FOR CROSS SECTION MEASUREMENTS

We have measured the quantities required for a calculation of the $W \to e\nu + \geq n$ jet cross sections. First, we calculate the number of $W \to e\nu + \geq n$ jet events produced at CDF during the period of data collection. This number is derived by correcting the number of $W \to e\nu + \geq n$ jet candidates for the contamination from backgrounds and for the loss of direct single $W \to e\nu + \geq n$ jet events (efficiency). The relative production is defined as the number of $W \to e\nu + \geq n$ jet events divided by the total number of $W \to e\nu$ events. The absolute cross sections will be obtained from the relative production rates by scaling to the inclusive $W \to e\nu$ cross section of $\sigma_0(W)\cdot BR(W \to e\nu\ ) = 2490 \pm 120$ pb as measured from a previous CDF analysis [24].

A. $W \to e\nu + \geq n$ Jet Cross Section Results

To calculate the number of $W \to e\nu$ events produced with at least n jets, we use the number of $W \to e\nu + \geq n$ jet candidates (N_n), subtract the estimated background contamination (B_n) to get the number of $W \to e\nu$ events in our candidate sample that were contributed from direct single W production. Dividing this difference by the efficiency (ϵ_n, estimated in section VI) of identifying a $W \to e\nu$ decay when the W is produced with n jets, we obtain a measurement of the number of $W \to e\nu$ events that were produced. The subscript indicates that these quantities are measured for each $W+ \geq n$ jet sample. For $n = 0$ this is the total (inclusive) number of direct single $W \to e\nu$ events. The fraction F_n is defined as the rate of $W \to e\nu + \geq n$ jet events relative to the total production rate. These fractions (F_n) are the relative production rates and they are presented in Table XIX. The inputs that were used in the determination of the relative production rates are also shown in the table.

The last step for obtaining cross sections is to scale the relative rates to the inclusive cross section times the branching ratio, which is from a previous CDF analysis that used the first 19.6 pb^{-1} of luminosity. The luminosity and vertex requirement efficiency were well measured for these data. The uncertainties in this measurement are retained in our absolute cross section measurements and represent a 4.8% uncertainty for each $W+ \geq n$ jet cross section. We refer to this contribution to the uncertainty as the common uncertainty. The cross sections for $W \to e\nu + \geq n$ jets are presented in Table XX and plotted in Figure 13. The curve in Figure 13 is an exponential fit to the data. The uncertainties in Table XX are divided according to type; the first uncertainty listed in the Table XX is statistical, the second is the common uncertainty (4.8%), and the third is the systematic uncertainty.

The systematic uncertainty dominates the uncertainties in the $W+$ jet measurements. An estimate of the systematic uncertaity must avoid double counting the uncertainties that are already accounted for in the common uncertainty. This is achieved by defining the systematic uncertainty to represent only the uncertainty on the ratio of $W+ \geq n$ jet events to $W+ \geq 0$ jet events. We discuss the quantities that can change the ratio in section VII B. Here, we only note that the dominant contribution is due to the uncertainty on the jet energy.

Also shown in Table XX is the ratio

$$R_{n/(n-1)} = \frac{\sigma_n}{\sigma_{n-1}}$$

$R_{n/(n-1)}$ shows explicitly that the cross section drops a factor of 5.2 ± 0.3 with each additional jet. This ratio gives the probability of measuring one additional jet in a W event and is therefore closely related to the coupling strength of the strong interaction α_s. In section IX A, we use $R_{n/(n-1)}$ to make more demanding tests of QCD since the uncertainty on this ratio is smaller than the uncertainty on the absolute cross section. The cancellation of the systematic uncertainty is predominately due to the correlation in the jet counting uncertainties in the numerator and denominator of $R_{n/(n-1)}$. For example, the increase in the number of jets from a shift in the jet energy increases both σ_n and σ_{n-1}. The increase in cross section is greater for higher jet multiplicities so that the cancellation is not complete but the final uncertainty is relatively smaller when compared to the absolute cross sections. This argument is not true in the ratio $\frac{\sigma_1}{\sigma_0}$ because σ_0 is insensitive to the jet counting uncertainties. We describe the systematic uncertainties in more detail in the next section.

TABLE XIX. Candidates, total background, total W efficiency (exclusive), and the relative cross sections for the $W+$ jet samples.

	≥ 0 jets	≥ 1 jet	≥ 2 jets	≥ 3 jets	≥ 4 jets
N_n	51431	11144	2596	580	126
B_n	3024	2102	686	210	66.7
ϵ_n	0.196	0.193	0.187	0.204	0.195
F_n	1.0000	0.1868	0.0395	0.0076	0.0012

TABLE XX. $W+\geq n$ jet Cross Sections. The total uncertainty is broken down into the combined statistical uncertainty (which includes the statistical uncertainty on the number of events and the statistical uncertainty on the efficiency and background calculations), the common systematic uncertainty (4.8% from the input inclusive W cross section), and the systematic uncertainty (which is dominated by jet counting systematics, see section VII B). For this table we list the maximum of the plus and minus systematic.

n	Cross Sections Results (pb)				σ_n
Jets	$BR \cdot \sigma$	Stat.	Com.	Syst.	$\overline{\sigma_{n-1}}$
≥ 1	471.2 ± 57.1	6.3	23.1	51.8	0.189 ± 0.021
≥ 2	100.9 ± 19.0	3.2	4.9	18.1	0.214 ± 0.015
≥ 3	18.4 ± 5.3	1.4	0.9	5.1	0.182 ± 0.020
≥ 4	3.1 ± 1.4	0.7	0.1	1.2	0.166 ± 0.042

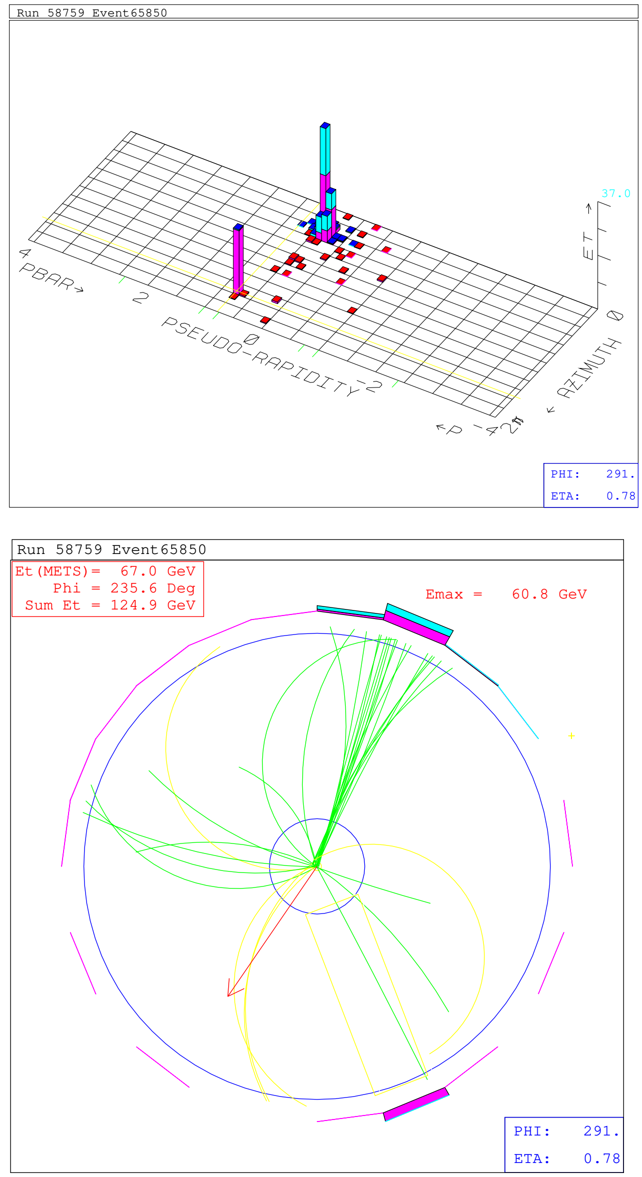

FIG. 6. The upper plot shows the energy deposited into the calorimeter from a $W+$ 1 jet event. The electron is located at $\phi = 291°$ and $\eta = 0.78$. The other tower cluster contains the jet's energy deposited in the electromagnetic calorimeter (dark shade) and the hadronic calorimeter (light shaded). The lower plot shows a view of the central tracking chamber. The beam line is perpendicular to the page. The track cluster associated with the calorimeter cluster is evident. The electron track is located in the dotted rectangle. A superimposed arrow indicates the direction of the missing transverse energy.

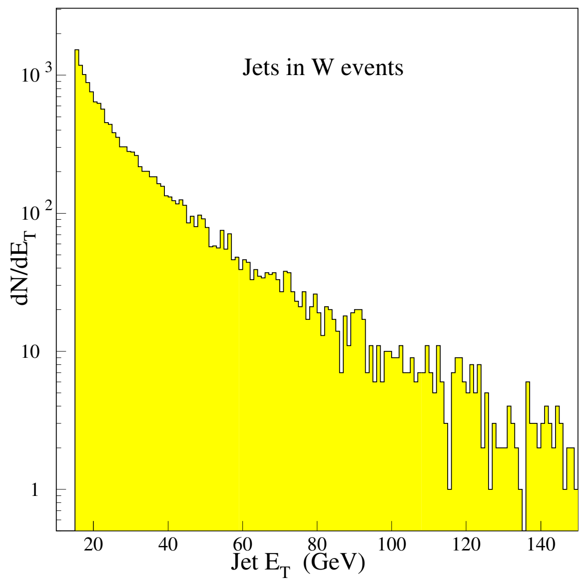

FIG. 7. The E_T distribution for all jets in the W sample with a $E_T \geq 15$ GeV.

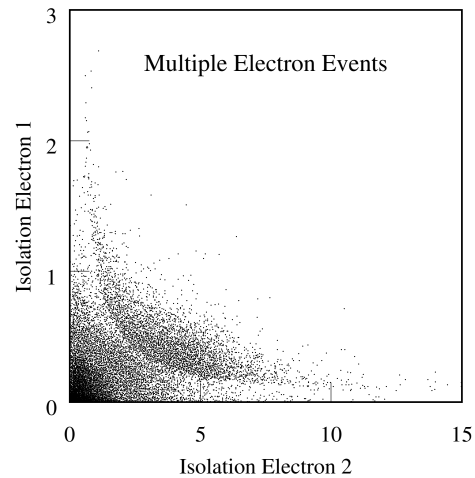

FIG. 9. The isolation of electron 1 versus isolation of electron 2 for events with at least two electrons. The events that show the inverse relation between electron isolations are events where the two electron clusters are closer than the cone used to define the isolation. We remove these events from the QCD sample because they do not contaminate the W sample.

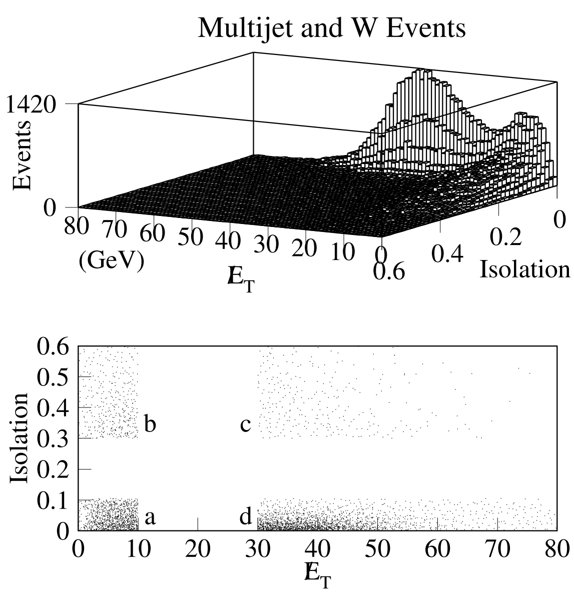

FIG. 8. Isolation vs $\not{E}_T$ for the QCD sample. The bottom plot shows the 3 regions (a,b, and c) which are used to calculate the QCD events in region d where W bosons dominate. The characteristic $\not{E}_T$ distribution of $W \rightarrow e\nu$ events is evident in the lego plot (top). The QCD events have a $\not{E}_T$ distribution that peaks near 0 in this plot.

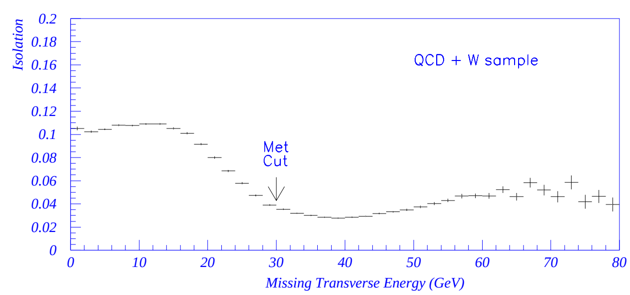

FIG. 10. A profile plot of isolation versus missing transverse energy. The vertical axis shows the average isolation for events with a particular $\not{E}_T$ (horizontal axis). The high missing energy events show the low isolation characteristic of W electrons but significant QCD contamination is evident up to our $\not{E}_T$ requirement of 30 GeV. The isolation of the low missing energy events are not completely independent of missing energy.

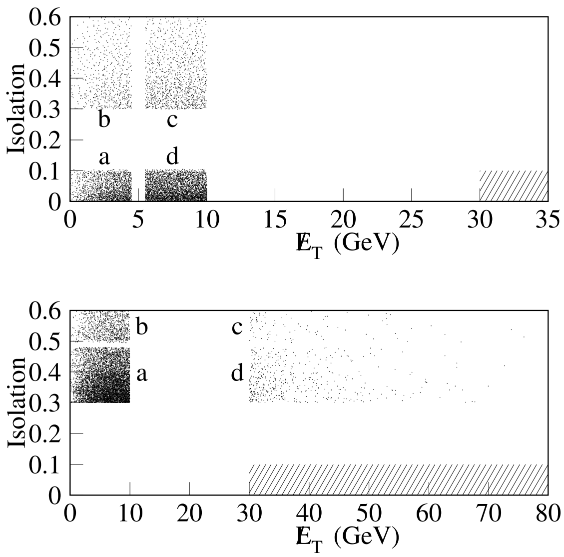

FIG. 11. The plots show the subsamples of events in the isolation-$\not E_T$ plane which are used to test the QCD calculation. The upper plot is the subsample of QCD events with low $\not E_T$ sample. The lower is the subsample with a poorly-isolated electron. Each sample is divided into 4 regions to allow a calculation of the events in region d which is compared to the number of events (N_d) observed in the region. These samples are chosen to be displaced from the W dominant region (indicated by cross hatching).

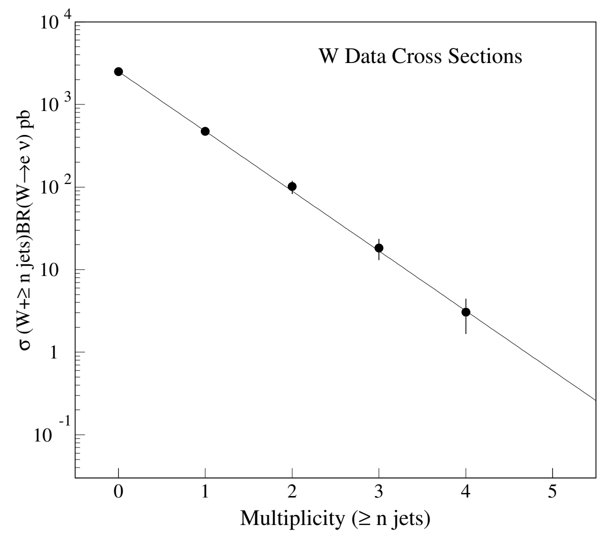

FIG. 13. $W+\geq n$ jets cross sections. The inclusive ($W+ \geq 0$ jet) cross section is from a previous CDF measurement. The fit line is an exponential that corresponds to the cross section dropping by 5.2 ± 0.3 for each additional jet.

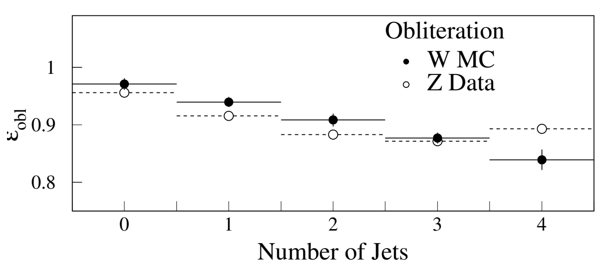

FIG. 12. Obliteration efficiency as calculated from W Monte Carlo (filled circles) and Z data (open circles). Statistical errors only; note that the systematic errors are large for the high-multiplicity points based upon the Z data because of the limited number of high-multiplicity Z events.

TABLE XXI. List of systematic uncertainties for $W+$ jets analysis. Values are in picobarns.

	$W+\geq 1$ Jet		$W+\geq 2$ Jets		$W+\geq 3$ Jets		$W+\geq 4$ Jets	
	$-\sigma$	$+\sigma$	$-\sigma$	$+\sigma$	$-\sigma$	$+\sigma$	$-\sigma$	$+\sigma$
E_T scale	−31.5	31.8	−10.1	11.5	−2.35	3.08	−0.53	0.70
η_{det}	−10.7	9.1	−4.1	3.7	−0.99	0.89	−0.41	0.17
Underlying Event	−23.0	27.3	−8.6	9.9	−1.91	3.01	−0.48	0.65
Promotion	−12.1	24.7	−3.7	7.2	−0.97	1.81	−0.24	0.44
QCD	−15.1	14.9	−5.6	5.5	−1.71	1.68	−0.49	0.49
Top	−0.24	0.24	−0.28	0.28	−0.24	0.24	−0.17	0.17
Acceptance	−3.58	3.64	−1.02	1.05	−0.32	0.34	−0.10	0.11
Obliteration	−0.97	0.97	−0.30	0.30	−0.11	0.11	−0.04	0.04

B. Systematic Uncertainties in the Data

In this section we give descriptions of the systematic uncertainties in the $W+$ jets analysis. The determination of a particular systematic is produced by varying a quantity by its uncertainty and recalculating the cross section. The difference of the new cross section and default cross section yields the systematic uncertainty on the cross section. The systematic variations we examine are those that change the ratio of the number of events with $\geq n$ jets to the total number of events.

The quantities which are varied systematically can be grouped into jet counting variations, backgrounds, and efficiencies. The jet counting variations are the jet E_T, the detector η cut, the underlying event energy scale, and the promotion correction. The background variations include the QCD background normalization and the top background normalization. The efficiency variations include the acceptance and the electron-jet overlap calculation.

The uncertainty on each of these quantities is explained more fully in the associated sections. Table XXI shows the change in the cross sections as a result of the variations that are listed above. The systematic error due to the uncertainty on jet counting dominates in all $\geq n$ jet samples. The counting error is in turn dominated by the uncertainty of the jet E_T. However, the contribution of systematic uncertainty due to extra interactions is also significant. The effect of extra interactions is seen in two uncertainties: the uncertainty on the correction of jet energy due to contamination of 0.4 clustering cone from extra interaction energy, and the uncertainty on the promotion correction which corrects for jets from extra interactions. As the instantaneous luminosity at CDF increases both the extra interaction correction and the promotion correction contribute a larger fraction of the total uncertainty. This point needs to be considered in future analyses which will collect data at even higher instantaneous luminosities.

VIII. PREDICTIONS FOR W BOSON PLUS JETS PRODUCTION

Generating perturbative QCD predictions requires several inputs which must be chosen with reasonable attention to both theoretical and experimental considerations. The leading order $W+$ parton calculations are most sensitive to the renormalization scale used in the evaluation of the strong coupling of the theory. We assess the dependence of the LO perturbative calculation on this scale and on other inputs.

Perturbative QCD yields definite predictions for the $W+$ parton cross sections. In order to compare theory to data at the level of jets, the partons need to be converted into jets. In a procedure we call enhanced leading order (ELO), we use the HERWIG parton shower simulation which fragments the parton and hadronizes the final state quarks. This procedures provides gluon radiation from both the initial state and final state partons. The degree to which HERWIG adds radiation is determined by the fragmentation scale. As one might expect, the cross section predictions are fairly insensitive to this scale but the kinematic predictions show some dependence as we shall see.

A. Event Generation

We use the program VECBOS [22], a leading order $W(Z)+$ parton Monte Carlo event generator, to produce the $W \to e\nu + n$ parton event samples. For $n=$ 1,2,3 and 4, we generate samples of 50000 events using the generation requirements listed in Section VI A 2.

The leading order matrix element calculation uses a two-loop (NLO) evolution of α_s chosen for consistency with the NLO order parton distribution function (CTEQ3M) [25]. We evaluate α_s at two renormalization scales that bracket the W boson mass. These scales are defined by equations 10 and 11 below. The value of α_s as a function of the renormalization scale is shown in Figure 14.

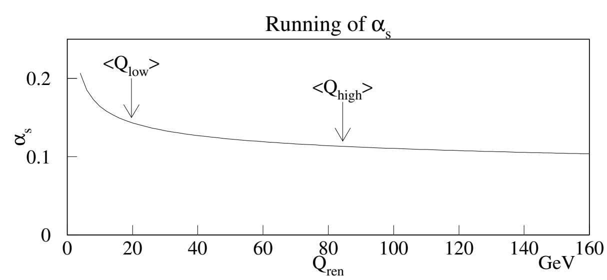

FIG. 14. The variation of strong coupling (α_s, two-loop) with the renormalization scale used in the VECBOS generator. The value of α_s for the two renormalization scales that are used in the LO matrix element calculation are indicated by the arrows.

The low renormalization scale is defined by the average value of the parton P_T. Explicitly, the lower renormalization scale is the scalar sum of the parton P_T's divided by the number of partons (n). The value of the lower renormalization scale is on average approximately $\frac{M_W}{4}$. The high renormalization scale is defined by the square root of the sum of the squares of the bosons mass and P_T. The average value of this quantity is about 84 GeV.

$$Q^2_{\text{REN}\ low} = < P_T >^2 = (\frac{\sum P_{Ti}}{n})^2 \qquad (10)$$

$$Q^2_{\text{REN}\ high} = M_w^2 + P_{TW}^2 \qquad (11)$$

The lower scale has several features that distinguish it from the higher scale. First, since it is on average less than 1/4 of the higher scale, the value of α_s is larger. The cross sections for the lower renormalization scale will be greater. Additionally, the decrease of the cross sections as a function of jet multiplicity will depend on the renormalization scale since the power of α_s is n. Finally, the lower renormalization scale varies with the parton P_T which can vary by an order of magnitude from event to event, while the higher scale is more or less a constant because the W boson invariant mass is large and fairly constant. This last distinction will primarily be reflected in the shapes of the kinematic variables that we examine. We will see that the differences in the higher and lower renormalization scales do not have a large effect on these shapes so that the kinematic variables provide stringent tests of QCD predictions.

The factorization scale is the scale used to evaluate the proton structure as defined by the parton distribution functions. This scale is always set equal to the renormalization scale for the $W+$ n parton predictions. The sensitivity of the cross section prediction to the factorization scale is much less than the sensitivity to the renormalization scale.

Although the VECBOS parton calculations are not compared directly to data, it is interesting to explore the dependency of the kinematic predictions on the various inputs to the theory. This allows us to see the effects of the LO scales factorized from the enhancements which are described in the next section. Figure 15 compares the $W+$ 1 parton predictions for the parton P_T distribution. The comparison is made for changes in the renormalization scale, the factorization scale and the parton distribution function. The renormalization scale has a noticeable effect on the parton P_T shape especially at low P_T as seen by the changing ratio at low P_T in the top plot of Figure 15. This is expected because the lower renormalization scale is in a region where α_s changes more rapidly (Figure 14). For the 1 parton sample that is plotted in Figure 15, there is an exact correlation between the parton P_T and the renormalization scale.

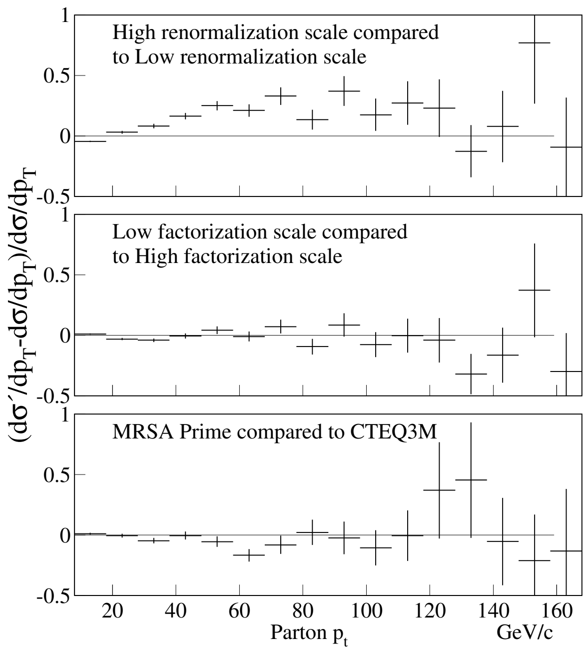

FIG. 15. Comparison of the parton P_T distributions for various $W+$ 1 parton VECBOS Monte Carlo samples. The plots shows (theory$'$-theory)/theory as a function of parton P_T. The default calculation uses $Q^2_{ren} = Q^2_{fac} =< P_t >^2$. This sample is compared to a sample derived from the high renormalization scale $Q^2_{ren} = M^2_W + P^2_{TW}$ (top), the high factorization scale $Q^2_{ren} = M^2_W + P^2_{TW}$ (middle) and an alternate PDF MRSA$'$ (bottom).

B. Fragmentation and Hadronization

The jet energy corrections in the $W+$ jet data analysis are designed to correct jets back to the parent-parton energy. Ideally we would compare the data results to the VECBOS predictions; however, parton fragmentation effects and measurement resolution must be included for a valid comparison.

We use the HERWIG [23] parton shower simulation to enhance the LO QCD calculation from VECBOS. HERWIG provides a color-coherent shower evolution which includes both initial- and final-state gluon radiation. HERWIG hadronizes the final quarks, and includes a data-based soft underlying event model.

The radiated gluon transverse momentum in HERWIG is limited by an input parameter in addition to kinematic considerations. We will refer to this parameter as the fragmentation scale, and its default value is the VECBOS QCD renormalization scale, used in computation of the running strong coupling constant α_s in the LO matrix element calculation. Using a low value for the fragmentation scale, such as the average parton P_T, results in a softer gluon distribution than is obtained using a larger value like the boson mass.

Gluon emission from VECBOS partons can have different effects, depending on the P_T of the radiated gluon and the resulting parent parton, and their separation ΔR in $\eta - \phi$ space. An additional jet is produced if a radiated gluon and the resulting parent parton are both energetic enough and their separation ΔR is large enough to pass jet clustering cuts. The VECBOS $W + n$ jet event is promoted to a $W+ \geq n$ jet event and it is kept in the sample since we treat the VECBOS sample as a LO inclusive $W + n$ jet generator. If the separation ΔR is less than the jet clustering criteria, then the parton and the radiated gluon will be clustered together into a single jet. However, if the separation between the initial parton and the radiated gluon exceeds the jet clustering cone size, and if both jets fall below the jet E_T threshold, then the event will have fewer than n jets and the event will be discarded, since it is no longer a member of the inclusive $W + n$ jet sample.

C. Enhanced Leading Order Predictions

The parton shower simulated by HERWIG represents a partial higher-order correction to the leading-order VECBOS calculations, so we call the combination enhanced leading order (ELO). We generate VECBOS samples with both low and high renormalization scales and for both samples pass them through the HERWIG simulation with a low and a high fragmentation scale. The resulting Monte Carlo data samples can be compared to the physics data to investigate the effects of the choice of parameters on the models' ability to reproduce the jet physics.

The ELO $W+ \geq n$ jet cross sections are presented in Table XXII for both the hard and soft fragmentation scales. The $W+ \geq n$ jet cross sections were measured by counting the number of events with at least n jets that have a $E_T \geq 15$ GeV and an $|\eta| \leq 2.4$. The jets from the HERWIG output were first processed with a detector simulation (QFL) to model the detector jet acceptance, jet energy response and jet energy resolution. The reconstruction of jet energy in the simulated Monte Carlo is identical to the algorithm used in the data.

TABLE XXII. Enhanced LO $W+ \geq n$ jet cross section predictions in picobarns. The results are presented for n=1 to 4 with statistical uncertainties shown. The determination of the cross section counted jets with a $E_T \geq 15.0$ GeV and an $|\eta_{det}| \leq 2.4$ after a full detector simulation of the jets had been performed.

$Q^2_{ren} = Q^2_{fac}$	$< P_T >^2$	$< P_T >^2$	$M^2_W + P^2_{TW}$
Q^2_{frg}	$M^2_W + P^2_{TW}$	$< P_T >^2$	$M^2_W + P^2_{TW}$
$W+ \geq 1$ jet	367 ± 5	316 ± 5	285 ± 4
$W+ \geq 2$ jet	112 ± 5	80.8 ± 2.5	58.1 ± 1.0
$W+ \geq 3$ jet	27.2 ± 2.1	21.1 ± 1.3	12.3 ± 0.62
$W+ \geq 4$ jet	5.81 ± 0.77	–	2.29 ± 0.21

IX. COMPARISONS OF THEORY TO DATA

A. Cross Section Comparisons

The $W \rightarrow e\nu$ + jet measured cross sections and the theory predictions for these cross sections are plotted in Figure 16. The errors on the data points are the sum of the statistical and systematic uncertainties. The sensitivity to the renormalization scale is indicated by the band

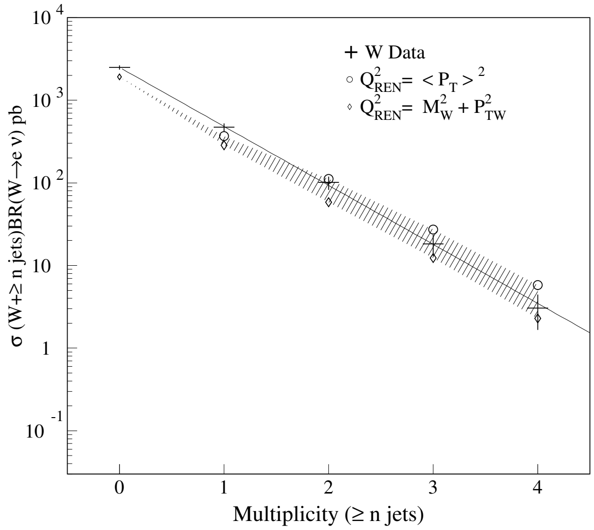

FIG. 16. $W + \geq n$ jets cross sections compared to theory. The horizontal lines are the data measurements with the error bars representing the combined statistical and systematic uncertainties. The band indicates the variation of the predictions with the renormalization scale. The $W+ \geq 0$ jet prediction is from a Born calculation of inclusive W production.

between the two theory predictions. The lower renormalization scale ($< P_T >^2$) yields higher cross sections as is expected since correlates with a higher value of α_s.

We have also plotted the leading order theory prediction for the inclusive W cross section ($W \rightarrow e\nu + \geq 0$ jets). Since jets have no effect on this point (α_s^0), there is no dependence on the renormalization scale. The uncertainty on the inclusive prediction is derived from the sensitivity to the factorization scale. The variation of this scale was from $\frac{M_W}{2}$ to $2M_W$ while the default value is M_W. The variation is not noticeable in the plot. This choice of factorization scale is consistent with the higher factorization scale ($\sqrt{(M^2_W + P^2_{TW})}$) that we use in the $W+$ jet predictions because the boson P_T is 0 for the born level calculation.

In Figure 17 we plot the ratio of data to theory cross sections versus the jet multiplicity. The upper plot shows the change in the theory predictions with the same renormalization scales from the previous cross section plot. This plot is to be compared with the lower plot in the same figure which shows the variation of the cross sections with the fragmentation scale. Clearly the fragmentation scale does not introduce large uncertainties into the cross section predictions when compared with the renormalization scale. The increase in cross section at a higher fragmentation scale is understood as the introduction of parton radiation from HERWIG that passes our jet selection criteria. These HERWIG jets can promote an event into the sample when the event contains a parton from the matrix element calculation that has failed

TABLE XXIII. Ratio of the measured cross sections to the predictions.

n Jets	$Q^2 = \langle p_T \rangle^2$ $\sigma_{\rm Data}/\sigma_{\rm QCD}$	$Q^2 = M_W^2 + p_{TW}^2$ $\sigma_{\rm Data}/\sigma_{\rm QCD}$
$\geq$1	1.28 $\pm$ 0.16	1.65 $\pm$ 0.20
$\geq$2	0.90 $\pm$ 0.17	1.74 $\pm$ 0.33
$\geq$3	0.67 $\pm$ 0.20	1.49 $\pm$ 0.44
$\geq$4	0.53 $\pm$ 0.25	1.33 $\pm$ 0.62

the jet requirements. The ratios of the measured cross section to the predicted cross sections are also presented in Table XXIII.

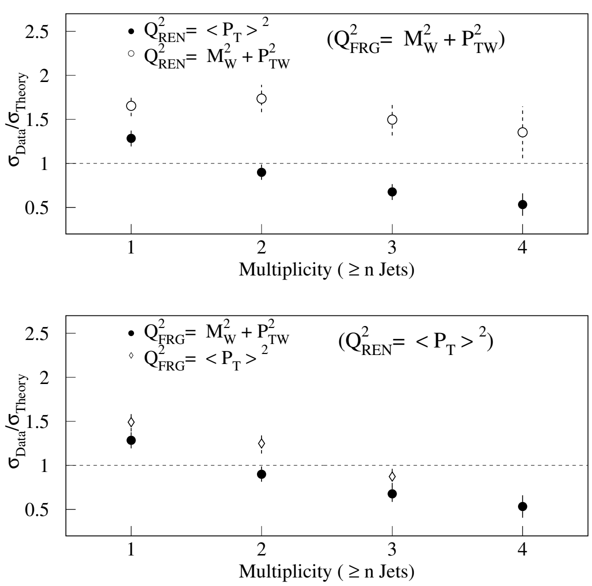

FIG. 17. The ratio of data to theory for the $W+ \geq$ n jet cross sections. The horizontal axis is the jet multiplicity. The upper figure compares the ratio for a variation in the renormalization scale. The lower plot shows the results for a variation in the fragmentation scale. The n= 4 point is unavailable for the lower fragmentation scale.

We show the ratio $R_{n/(n-1)}$=($\frac{\sigma_n}{\sigma_{n-1}}$) for the data and Monte Carlo at the top of Figure 18. The data measurement of this ratio benefits because the uncertainties are less than half the relative size of the cross section uncertainties except for R_{10} where the jet counting systematics will not cancel. We also see that $R_{n/(n-1)}$ is more robust to the renormalization scale because variations cancel in the ratio.

The particular value of $R_{n/(n-1)}$ will vary as function of the specific jet E_T requirement that defines a jet. The jet definition we chose is jet $E_T \geq$ 15 GeV. To remove this dependence to some degree we plot in Figure 18 (bottom) the ratio of data and theory for $R_{n/(n-1)}$. With accurate theory predictions and accurate data measurements the value of this ratio is 1.0. The predictions and measurements are in fair agreement for this quantity. If the QCD predictions reproduce the jet kinematics accurately the ratio of data to theory is independent of the choice of jet E_T requirement so that the quantity may be of more general interest. Although we have measured this ratio for only one jet E_T definition for each $W+$ jet sample, we examine the performance of QCD kinematic predictions through alternate tests in section IX B.

Interpreting the data and theory comparisons that were just described, we see that the absolute cross section predictions agree with the data for n=2 through 4. The $W+ \geq$ 1 jet data cross section is a factor of 1.3 high for $Q^2_{\rm REN} = < P_T >^2$ and a factor 1.7 high for $Q^2_{\rm REN} = M_W^2 + P_{TW}^2$. The lower renormalization scale agrees better in magnitude, while the higher scale agrees better with the slope of cross section versus the number of jets. The variation of the cross section predictions with the renormalization scale indicates that higher order corrections to the LO $\geq$ 1 jet cross section could be of the order of 30%. The QCD corrections to the inclusive prediction are known to be about 20%. Therefore, the lack of quantitative agreement is not a serious concern. The QCD predictions of the absolute cross sections are in agreement with the data given the inherent uncertainty of LO QCD.

The $R_{n/(n-1)}$ comparison (Figure 18) is valid if higher order QCD corrections to the LO cross sections are not strongly dependent on the number of final state partons (i.e. the order of α_s). The ratio $R_{n/(n-1)}$ measures the decrease in cross section with the addition of 1 jet. Although not a direct measure of α_s, the value of $R_{n/(n-1)}$ is clearly dictated by the magnitude of the strong coupling since adding an extra jet adds a factor of α_s. Figure 18 shows that this ratio is well predicted by QCD and the lower value of α_s is favored by the data (see Figure 14). This value yields roughly a factor of 5 decrease in the cross section with each additional jet. This decrease in the data actually may show some dependence with the number of jets which is clearly evident in the theory.

B. Kinematic Distributions

The kinematic distributions we study include various jet E_T, mass and angular variables. These distributions have been measured from the $W+$ jet data but were not corrected for variations in the efficiency of W boson identification as a function of the variable that we study. In order to make a fair comparison we must include this differential efficiency in the theory. This is achieved with the use of a full detector simulation that models the response to all final state particles from $W \rightarrow e\nu$ + jet production. For these fully simulated events we apply our

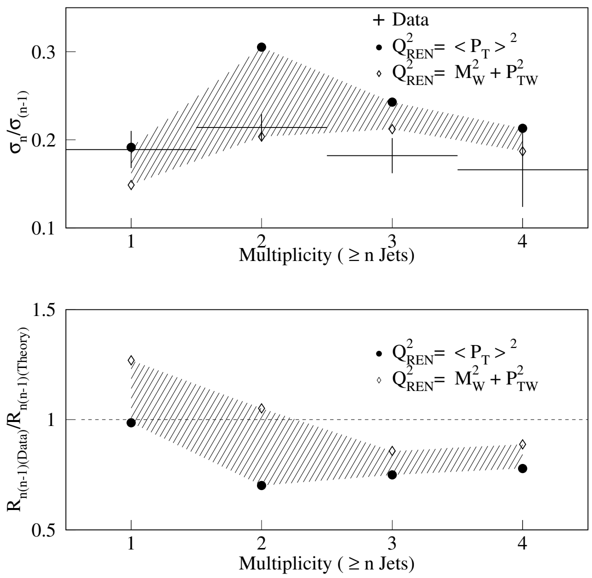

FIG. 18. The upper plot shows data and theory comparisons for σ_n/σ_{n-1}. The band represents the variation with the renormalization scale. The error bars on the data represent the combined statistical and systematic uncertainty. The lower plot shows the ratio of data to theory of the quantity σ_n/σ_{n-1}. The horizontal axis for both plots is the jet multiplicity.

full W selection procedure in order to include the biases from the use of electron and neutrino requirements.

Before the data are compared to theory, the $W+$ jet kinematic distributions are corrected for the backgrounds that change the shape of the jet spectra. There are three significant backgrounds: promotions, QCD, and top. The top quark contributions are only important in the $W+\geq 4$ jet distributions. The promotion backgrounds (photons and jets from extra interactions) generally contribute jets at the lowest transverse energies so that that they have a concentrated effect on the jet E_T spectra. Likewise, the QCD background has a significant effect on the low region of the E_T spectra but this is due to a deficit of QCD contribution in this region rather than an excess.

We show in Figure 19 a shape comparison between the W^+ and W^- data for distribution of the highest E_T jet in an event. The plot shows the fractional difference in the contribution to each bin of the E_T distribution by $W^+ +$ jet events and $W^- +$ jet events. The distributions should be consistent because there is no known physics which could change the shape of one distribution without changing the other. Thus the comparison of Figure 19 could indicate η asymmetries in the detector's jet acceptance since W^+'s are produced preferentially in the direction of the proton and W^-'s are produced preferentially in the direction of the antiproton. In Figure 20 the same distribution is compared for W and Z data (The Z data is normalized to the W data for this distribution). In this comparison, the jet E_T and background systematics cancel except for the QCD background which is negligible in the Z data. There was small but noticeable improvement after correcting the W data for the QCD contribution. LO QCD predicts that the W and Z jet E_T distributions [26] are very similar and we observe this in Figure 20.

Finally, before we compare data to theory we normalize the theory distributions to the total number of events in the data. The kinematic tests of the theory will therefore explicitly reveal the sensitivity of the kinematic shapes to the QCD parameters that we used as input. The systematic uncertainties in the data distributions are also calculated to only represent the change in the shape of the distributions.

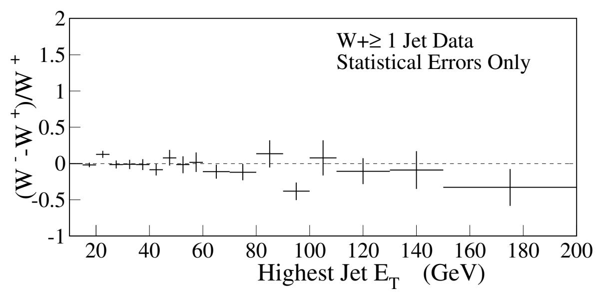

FIG. 19. The plot compares the jet E_T distributions for the highest E_T jet found in W^+ events and W^- events. The vertical axis represents the fractional difference of events per bin of E_T. The samples are normalized in area to one another before a comparison is made.

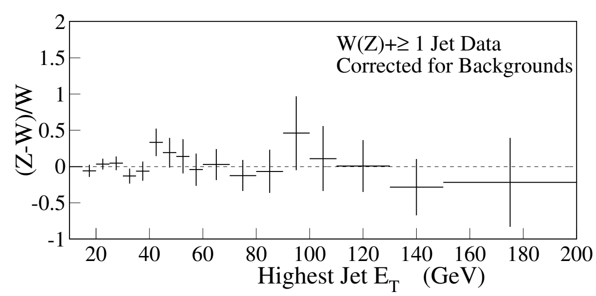

FIG. 20. The plot compares the jet E_T distributions for the highest E_T jet found in W and Z events. The vertical axis represents the fractional difference of events per bin of E_T. The samples are normalized in area to one another before a comparison is made.

1. Jet Transverse Energy

We compare data to theory in Figure 21 for the E_T of the highest E_T jet in $W+\geq 1$ jet events, the second highest E_T jet in $W+\geq 2$ jet events, the third highest E_T jet in $W+\geq 3$ jet events, and the fourth highest E_T jet in $W+\geq 4$ jet events. The solid curves are theory for the low renormalization scale and the dashed curves are theory for the high renormalization scale. The curves are fits of an analytic function to the theory histograms. The analytic function was chosen exclusively on its ability to reproduce the theoretical distributions via a minimum χ^2 test.

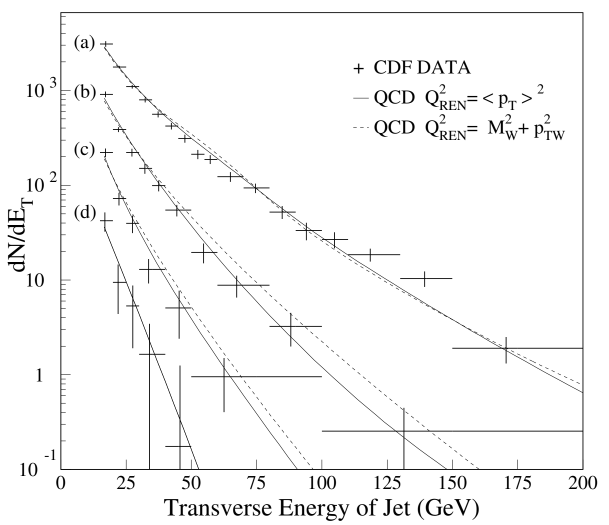

FIG. 21. The jet E_T distribution for (a) the highest E_T jet in $W+\geq 1$ jet events, (b) the second highest E_T jet in $W+\geq 2$ jet events, (c) the third highest E_T jet in $W+\geq 3$ jet events, (d) the fourth highest E_T jet in $W+\geq 4$ jet events. The points represent the data and the curves represent the theory. The solid curve is for the lower renormalization scale and the dashed is for the higher renormalization scale. The curves were derived from fits to an analytic function that reproduced the theory well.

We can see in Figure 21 that the sensitivity of the theory to the renormalization scale is mild with respect to the variations in the cross section predictions. However, we expect that the lower renormalization scale yields a softer E_T spectrum because the lower scale weights low E_T events more than the high E_T events.

The details of the data and theory comparison for the ≥ 1 jet sample are better seen in Figure 22. This plot shows (data $-$ theory)/theory using the low renormalization scale. The error bars represent the statistical uncertainty while the band represents the systematic uncertainty on the data due to the background corrections and the jet energy uncertainty. We notice deficits in the theory at low E_T and high E_T. The low E_T and high E_T regions of the jet E_T distribution are regions where we expect the theory to be sensitive to higher order corrections.

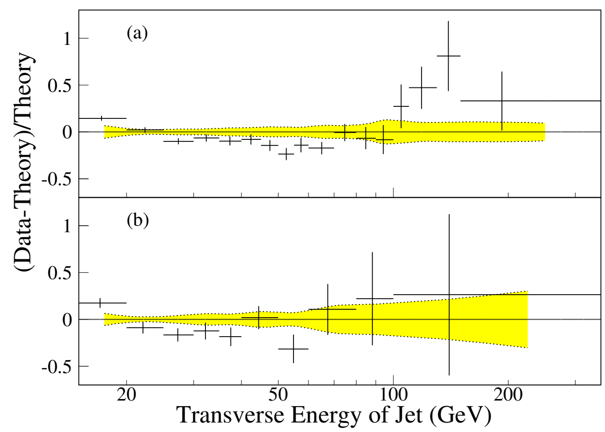

FIG. 22. Comparison of jet E_T distributions between data and theory. The fractional difference ((data-theory)/theory) versus the E_T of the highest E_T jet in $W+\geq 1$ jet events (a) and second highest E_T jet in $W+\geq 2$ jet events (b). The theory uses $Q^2 = <P_T>^2$ and is normalized to the data before comparison.

A detailed examination of the $W+\geq 1$ jet E_T distribution reveals several important features. Specifically, the ratio is flat between about 30 GeV and 100 GeV, indicating that the theory accurately predicts the shape of the data in this region. The offset from 0 is caused by the normalization and the deficit of events in the theory outside of this range. One limitation of the theory that causes this deficit can be seen in Figure 23 which plots the fraction of events with exactly 1 jet as a function of the E_T of the highest E_T jet. In the data, as the jet E_T increases, the number of events with exactly 1 jet decreases. In other words, this distribution partially discriminates events based on the their jet multiplicity. In the region where the theory shows a deficit, above 100 GeV, the ≥ 2 jet events are dominant. Therefore we expect that higher order corrections will be significant in this high E_T region.

Partial higher order corrections are provided by the HERWIG parton shower model. Multijet events in the theory receive the extra jets from HERWIG added radiation. Figure 23 also shows the 1-jet fraction for the theory. The first feature to notice is that the addition of HERWIG radiation decreases the fraction of 1-jet events just as in the data. A LO 1-parton calculation alone can not reproduce this feature. The second feature to notice is that the partial higher order corrections provided by HERWIG begin to fail at about the W boson mass energy. The flattening of the 1-jet fraction at high jet E_T can be partially related to the fragmentation scale which limits the energy of the added radiation.

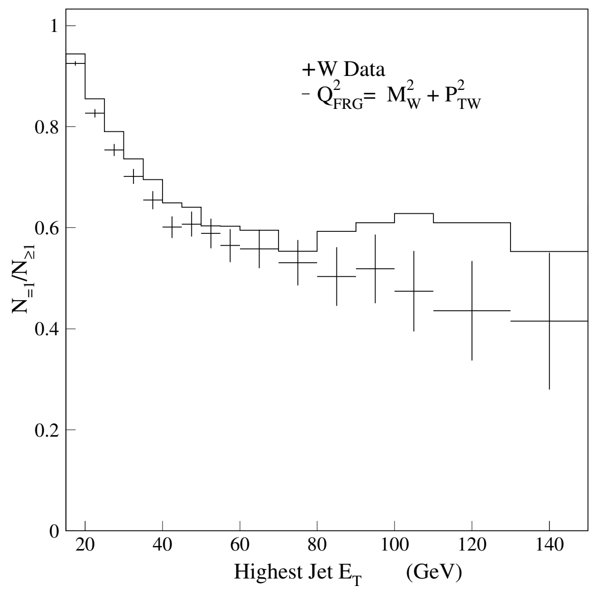

FIG. 23. The fraction of =1 jet events in $\geq$ 1 jet events versus the E_T of the highest E_T jet.

The fragmentation scale we use is a high scale and is equal to $\sqrt{(M_W^2 + P_{TW}^2)}$. The variation of the fragmentation scale was examined in the previous $Z+$ jet analysis [26] where high ($\sqrt{M_W^2 + P_{TW}^2}$) and low ($\sqrt{(< P_T >^2)}$) scales were tested with the $Z+$ jet kinematic distributions. The results favored the higher scale in reproducing the angular distributions of jets in Z events. We examine the effect of the higher fragmentation scale on the comparison of the $W+$ jet E_T distributions by looking directly at the E_T distribution of the jets produced by HERWIG. Figure 24 shows the E_T of the highest HERWIG-jet in the $W+ \geq 1$ jet Monte Carlo. The results are shown for the default fragmentation scale and for (effectively) unlimited added gluon radiation. The two scales show agreement up to an energy equivalent of the W mass which is where HERWIG begins to limit the radiation in our predictions. Although the unlimited fragmentation scale better reproduces the data (*i.e.*, it would partially correct the theory curve in figure 23), there remains a deficit of events in the high E_T region. Additionally, the choice to add unlimited radiation is not guided by any physics scales in the $W+$ jet events. A more coherent approach would be to obtain the true higher order corrections for the $W+$ 1 jet calculations.

The shape of the jet E_T distribution at low jet E_T is sensitive to backgrounds and the jet energy scale uncertainty. We have studied the variation of the shape due to these effects and find that they can not account for all of the deficit in the theory (Figure 22). The shape of theory distribution is also sensitive in this region for two reasons. The added initial state radiation can have a higher E_T than that from the jet initiated from matrix-element parton. This introduces a sensitivity to the fragmentation scale, particularly in regions where the matrix element parton P_T is low. Additionally, hard HERWIG radiation can not only supersede the matrix-element parton but can promote an event into the sample which previously would be rejected due to the low P_T of the matrix-element parton. This effect introduces an ambiguity in the parton P_T requirement used to generate the LO calculation. All of these effects are smaller above 25 GeV and the data and theory are in good agreement, noting that the data below 25 GeV has affected the normalization of the points above 25 GeV.

Summarizing the comparisons of data to theory for the jet E_T distributions, we see that the theory reproduces the data over a large range of jet E_T for all jet multiplicities. Focusing on the $W+ \geq 1$ jet predictions, the theory accurately reproduces the data in those regions where we expect that higher order corrections are small. The partial higher order corrections provided by HERWIG are insufficient in the regions that are dominated by higher order QCD production mechanisms.

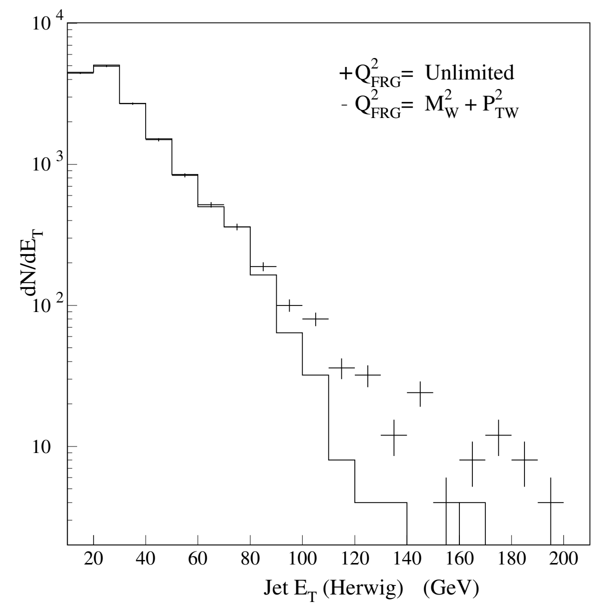

FIG. 24. E_T of highest E_T jet from HERWIG. The histogram shows the distribution with $Q^2_{\rm FRG}$=$M_W^2 + P_{TW}^2$. Here we used $Q^2_{\rm FRG}$ = $(300\text{GeV})^2$ which is essentially no limit on the radiation.

2. Angular and Mass Distributions

The angular correlations of jets are studied with two variables: the dijet invariant mass (M_{jj}) and the dijet angular separation (ΔR_{jj}). In Figure 25 we show the invariant mass of the two highest E_T jets in the $W+$

$\geq$ 2 jet sample (top-left) and the $W + \geq 3$ jet sample (bottom-left). On the right side of this figure is the jet-jet separation (ΔR_{jj}) for the two highest E_T jet events in the $W+ \geq 2$ jet sample (top) and $W+ \geq 3$ jet sample (bottom).

The dijet invariant mass spectra of Figure 25 are qualitatively well reproduced by the QCD predictions. We do note a harder mass spectrum for both renormalization scale choices. The distribution is better produced by the low renormalization scale. Since the mass distribution is not completely uncorrelated with the E_T distributions that were discussed earlier, a more reliable test of the angular correlations is given by the ΔR_{jj} distributions. The jet–jet separation is insensitive to the renormalization scale and shows excellent agreement with the data for both the $W+ \geq 2$ jet data and $W+ \geq 3$ jet data. Uncorrelated jets will peak at a value of ΔR_{jj} equal to about π. Therefore the low region of the ΔR_{jj} distribution provides the clearest test for QCD predictions. This region consists of 2 jets separated by a small angle. These are referred to as small angle jets. We can observe small angle jets to a small separation of 0.52 because we use the small clustering cone for identifying jet clusters. In Figure 25, we see that the theory predictions for the rate of small angle jets remains valid to the resolution limit of jet-jet separation for our analysis.

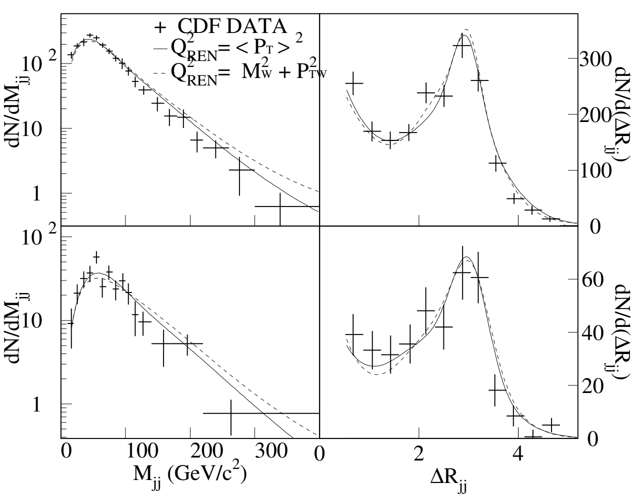

FIG. 25. The plots on the left show the distributions for the invariant mass of the two highest E_T jets in $W+ \geq 2$ jet events (top) and $W+ \geq 3$ jet events (bottom). The plots on the right show the separation (ΔR_{jj}) in $\eta - \phi$ space for the two highest E_T jets in $W+ \geq 2$ jet events (top) and $W+ \geq$ 3 jet events(bottom). $\Delta R_{jj} = (\Delta\phi^2 + \Delta\eta^2)^{1/2}$

X. CONCLUSIONS

We have measured $\sigma(W) \cdot BR(W \to e\nu)$ as a function of the jet multiplicity for W bosons produced in 1.8 TeV $\overline{p}p$ collisions. Generally, the ELO QCD predictions reproduced the main qualitative features of the data for cross sections and jet kinematics.

The $W+$ jet cross section measurements and jet kinematic distributions were directly compared to enhanced leading order QCD calculations of $W+$ jets. The comparisons show agreement between data and theory for the $W+ \geq n$ jet cross section measurements with $n \geq 2$. The n=1 predictions are low by a factor of 1.28 ± 0.16 ($< P_T >^2$) and 1.65 ± 0.20 ($M_W^2 + P_{TW}^2$). However, the large variations with the renormalization scale indicate that the higher order corrections to the LO cross sections are substantial.

The ratio of the $W+ \geq n$ jet cross section to the $W+ \geq (n-1)$ jet cross section ($\frac{\sigma_n}{\sigma_{n-1}}$) is measured more accurately than the absolute cross sections. For the data we find that the cross section drops by a factor of 5.2 ± 0.3 for each additional jet that we require. The predictions for this ratio have a smaller dependence on the renormalization scale than the predictions for the cross sections. Comparing the ratio removes the normalization difference between the data and theory and focuses on the influence of the strong coupling. The data and theory showed good agreement across all multiplicities where calculations were available (n=1 to 4) with the higher renormalization scale matching the data particularly well.

The enhanced leading order QCD predictions accurately reproduced the main features of jet kinematics. QCD properly predicted the rate of collinear jets to the smallest angles observed. As with the cross section comparisons the kinematic distributions indicated that some distributions could benefit from true higher order corrections. Specifically, the $W+ \geq 1$ jet data provided sufficient statistical accuracy for an examination of events with a highest jet E_T above 100 GeV. The highest E_T region is where one might expect perturbative QCD to perform best. It was shown that this region contained a high concentration of multijet events which require higher order QCD production diagrams for their description.

We thank the Fermilab staff and the technical staffs of the participating institutions for their vital contributions. We also thank Walter Giele for many useful discussions. This work was supported in part by the U.S. Department of Energy and the National Science Foundation, the Italian Istituto Nazionale di Fisica Nucleare, the Ministry of Science, Culture, and Education of Japan, the Alfred P. Sloan Foundation, and the Grainger Foundation.

[1] F. Abe *et al.*, Phys. Rev. Lett. **76**, 2015 (1996).
[2] F. Abe *et al.*, Phys. Rev. Lett. **70**, 4042 (1993).
[3] S. Abachi *et al.*, Phys. Rev. Lett. **75**, 3226 (1995).
[4] F. Abe *et al.*, Phys. Rev. Lett. **79**, 4760 (1997).
[5] F. Abe *et al.*, Phys. Rev. Lett. **75**, 1017 (1995).

[6] S. Abachi *et al.*, Phys. Rev. Lett. **75**, 1023 (1995).
[7] S. Abachi *et al.*, Phys. Rev. Lett. **77**, 3303 (1996).
[8] F. Abe *et al.*, Phys. Rev. D **51**, 4623 (1995).
[9] F. Abe *et al.*, Phys. Rev. Lett. **74**, 2626 (1995).
[10] S. Abachi *et al.*, Phys. Rev. Lett. **74**, 2632 (1995).
[11] D. Cronin-Hennessy, Ph.D. thesis, Duke University, Durham, NC 27708, 1998, also available at www.phy.duke.edu/research/hep/pubs/Hennessy_thesis.ps.
[12] F. Abe *et al.*, Nucl. Instrum. Methods Phys. Res., Sect. A **271**, 387 (1988).
[13] F. Abe *et al.*, Phys. Rev. D **44**, 29 (1991), our selection cuts are the same as those in this reference except for (i) $0.5 < E/p < 2.0$ and (ii) $\chi^2_{strip} < 10$.
[14] F. Abe *et al.*, Phys. Rev. D **45**, 1448 (1992).
[15] F. Abe *et al.*, Phys. Rev. D **47**, 4857 (1993).
[16] C. Caso *et al.*, The European Physical Journal C **3**, 1 (1998), 1999 off-year partial update for the 2000 edition available at http://pdg.lbl.gov/.
[17] T. Sjöstrand, Comput. Phys. Commun. **82**, 74 (1994).
[18] F. Abe *et al.*, Phys. Rev. Lett. **80**, 2773 (1998).
[19] F. Abe *et al.*, Phys. Rev. Lett. **82**, 271 (1999), erratum PRL 82, 2808.
[20] E. L. Berger and H. Contopanagos, Phys. Lett. B **361**, 115 (1995).
[21] S. Jadach *et al.*, Comput. Phys. Commun. **76**, 361 (1993).
[22] F.A. Berends, W.T. Giele, H. Kuijf, and B. Tausk, Nucl. Phys. B **357**, 32 (1991), see also *http://www-theory.fnal.gov/people/giele/vecbos.html*.
[23] G. Marchesini and B. Webber, Nucl. Phys. B **310**, 461 (1988).
[24] F. Abe *et al.*, Phys. Rev. Lett. **76**, 3070 (1996).
[25] H.L Lai and others, Phys. Rev. D **51**, 4763 (1995).
[26] F. Abe *et al.*, Phys. Rev. Lett. **77**, 448 (1996).